Additive Manufacturing 47 (2021) 102329

Contents lists available at ScienceDirect

Additive Manufacturing

journal homepage: www.elsevier.com/locate/addma

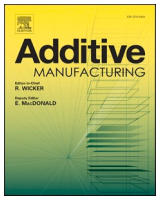

Research Paper

Comparison of microstructure, crystallographic texture, and mechanical properties in Ti–15Mo–5Zr–3Al alloys fabricated via electron and laser beam powder bed fusion technologies

Shi-Hai Sun [a,b,c], Koji Hagihara [a,b,d], Takuya Ishimoto [a,b], Ryoya Suganuma [a], Yun-Fei Xue [c], Takayoshi Nakano [a,b,*]

[a] Division of Materials and Manufacturing Science, Graduate School of Engineering, Osaka University, 2-1 Yamadaoka, Suita 565-0871, Japan
[b] Anisotropic Design & Additive Manufacturing Research Center, Osaka University, 2-1 Yamadaoka, Suita 565-0871, Japan
[c] School of Materials Science and Engineering, Beijing Institute of Technology, Beijing 100081, China
[d] Department of Physical Science and Engineering, Nagoya Institute of Technology, Gokiso, Nagoya 466-8555, Japan

ARTICLE INFO

Keywords:
Electron beam powder bed fusion
Laser powder bed fusion
Process map
Beta-Ti alloy
Crystallographic texture

ABSTRACT

Depending on the application, establishing a strategy for selecting the type of powder bed fusion technology—from electron beam (EB-PBF) or laser powder bed fusion (L-PBF)—is important. In this study, we focused on the β-type Ti–15Mo–5Zr–3Al alloy (expected for hard-tissue implant applications) as a model material, and we examined the variations in the microstructure, crystallographic texture, and resultant mechanical properties of specimens fabricated by L-PBF and EB-PBF. Because the melting mode transforms from the conduction mode to the keyhole mode with an increase in the energy density in L-PBF, the relative density of the L-PBF-built specimen decreases at higher energy densities, unlike that of the EB-PBF-built specimen. Although both EB-PBF and L-PBF can obtain cubic crystallographic textures via bidirectional scanning with a 90° rotation in each layer, the formation mechanisms of the textures were found to be different. The <100> texture in the build direction is mainly derived from the vertically grown columnar cells in EB-PBF, whereas it is derived from the vertically and horizontally grown columnar cells in L-PBF. Consequently, different textures were developed via bidirectional scanning without rotation in each layer: the <110> and <100> aligned textures along the build direction in L-PBF and EB-PBF, respectively. The L-PBF-built specimen exhibited considerably better ductility, but slightly lower strength than the EB-PBF-built specimen, under the conditions of the same crystallographic texture and relative density. We attributed this to the variation in the microstructures of the specimens; the formation of the α-phase was completely absent in the L-PBF-built specimen. The results demonstrate the importance of properly selecting the two technologies according to the material and its application.

1. Introduction

Electron beam powder bed fusion (EB-PBF) [1–5] and laser powder bed fusion (L-PBF) [1–4] are representative powder bed fusion additive manufacturing (AM) technologies used for metallic materials. Both technologies can produce components with high geometrical accuracy and good mechanical properties [1–5]. However, there exist several prominent differences between EB-PBF and L-PBF, as presented in Supplementary Table 1s, which must be considered when selecting between these two technologies for practical applications:

First, EB-PBF and L-PBF use electrons and laser beams as heat sources, respectively. The power of the EB-PBF is as high as 3 kW, and the energy usage efficiency of the electron beam is significantly high because of the high-energy transformation through electron and powder collisions and vacuum working conditions. Because a vacuum can reduce collisions between electrons and residual gas during the transfer process, even refractory metals and alloys can be easily melted [1–3,5]. The energy absorption of a laser beam relies on thermal radiation, which is significantly affected by the laser wavelength, temperature, materials, gas atmosphere, and surface morphology [6]. For example, the energy

* Corresponding author at: Division of Materials and Manufacturing Science, Graduate School of Engineering, Osaka University, 2-1 Yamadaoka, Suita 565-0871, Japan.
E-mail address: nakano@mat.eng.osaka-u.ac.jp (T. Nakano).

https://doi.org/10.1016/j.addma.2021.102329
Received 5 May 2021; Received in revised form 10 September 2021; Accepted 13 September 2021
Available online 28 September 2021

absorptivity of copper is as low as 2–3% for a Yb laser at 25 °C [7]. Therefore, obtaining the fully dense part of copper by L-PBF is considerably difficult, although the melting point of copper is lower than that of iron. In contrast, the copper part fabricated by EB-PBF exhibits a high density [8]. However, the electron beam is easily disturbed by the magnetic field, whereas the laser beam is not. Therefore, strong magnetic materials such as NdFeB, which are difficult to treat by EB-PBF, can be fabricated via L-PBF [9].

Second, the beam size is smaller in the L-PBF than in the EB-PBF. A smaller beam size in L-PBF can increase the processing accuracy. Conversely, a larger beam size in EB-PBF can produce a shallower and wider melt pool, thereby decreasing the porosity by preventing the void generated by the lack of overlap of the melt pools [10].

Third, a coarser powder (60–105 μm) is used in EB-PBF whereas a finer powder (10–60 μm) in L-PBF [2]. Thus, the surface roughness of L-PBF is generally lower than that of EB-PBF [11].

Fourth, the scanning speed during the melting process is higher in EB-PBF than in L-PBF [12]. Thus, the build speed of EB-PBF is often higher than that of L-PBF [4], although the additional preheating process in EB-PBF increases the production time. In addition, a larger layer thickness is employed in EB-PBF [1,4] because of the use of a coarser powder, which is another reason for the high build speed.

Fifth, EB-PBF works in a vacuum atmosphere with a lower partial pressure (0.2 Pa) of He gas during the melting process [1,3–5], whereas L-PBF works in an Ar or N_2 protection atmosphere with an O_2 content less than 0.1 vol% [1,3,4]. Therefore, oxidation of the powder can be more easily prevented in EB-PBF.

Finally, in EB-PBF, an additional preheating process is often carried out in each layer, wherein the powder is slightly sintered via a defocused beam with a high scanning speed to improve the conductivity of the powder and prevent a smoking phenomenon because of charge accumulation [1–5]. The preheating temperature is maintained at approximately 0.5–0.8 times the melting point of the material [1,4,5], which can reduce the residual stress, enabling control of the high-temperature microstructure in heat-resistant alloys, such as TiAl [13,14]. In the case of L-PBF, although the substrate can be heated up to 200 °C to increase the bonding between the build part and substrate, the residual stress in the L-PBF-built sample is still significantly large [15].

In addition to these differences between EB-PBF and L-PBF, the microstructures and resultant mechanical properties of the products

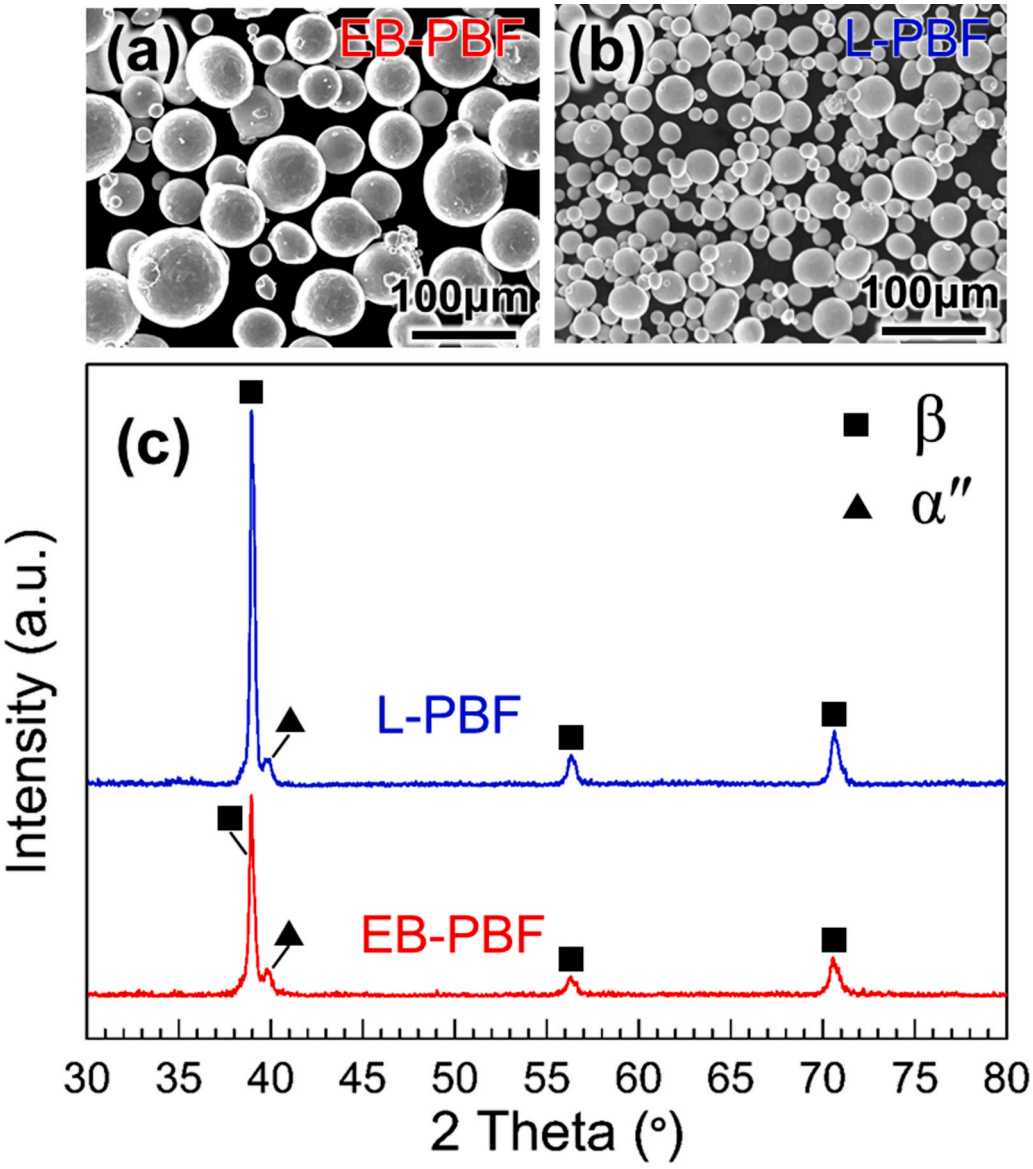

Fig. 1. Morphology of the powders used in (a) EB-PBF and (b) L-PBF and (c) X-ray diffraction profiles of the powders showing the constituent phase consisting of β-phase and a small amount of α″-phase.

fabricated using these technologies should be considered when selecting these two technologies to obtain excellent properties. Several researchers have indicated a preference for L-PBF-built materials to form single phases [16], martensite [17], nanosized precipitates [18,19], fine columnar cells [19], and more pores [16,17], compared to EB-PBF-built materials. Some L-PBF-built materials, such as Ti–6Al–4V [17] and stainless steel 316L [18], have been reported to exhibit higher strength and corrosion resistance, but lower ductility and shorter fatigue life than EB-PBF-built materials. The lower ductility in the L-PBF-built Ti–6Al–4V alloy and stainless steel 316L was attributed to the formation of brittle α′-phase and element-segregated subgrain structures, respectively. The shorter fatigue life in the L-PBF-built Ti–6Al–4V alloy and stainless steel 316L was reportedly related to pore formation and unmelted powders, respectively [17,18].

The abovementioned studies have compared the microstructures and mechanical properties of the components fabricated via EB-PBF and L-PBF without optimized building conditions, which is required to ensure a legitimate comparison. To obtain the optimized condition, establishing a process map—which demonstrates the variation in specific properties as a function of the process parameters—is effective.

In addition, the formation of a crystallographic texture is an important feature of AM [20–26], which can significantly affect the mechanical properties of the fabricated part [20–24]. Many studies have focused on the development of crystallographic texture during AM [20–26], but no systematic study has focused on the differences between EB-PBF and L-PBF using the same starting material.

In this study, we focused on the β-type Ti–15Mo–5Zr–3Al (wt%) alloy with body-centered cubic (bcc) structure as a representative material for comparing EB-PBF and L-PBF [27]. It is a promising material for hard tissue implants with low Young's modulus, and has been approved by the International Organization for Standardization (ISO 5832-14) [28,29]. Implants for hard tissue need to be adapted to the shape of the host bone and should also have Young's modulus as low as that of the human bone to prevent stress shielding [30], for better repair of bone injuries. These requirements can be simultaneously satisfied via AM technology because of its processing ability to make any shape and control the single-crystalline-like microstructure. Although Young's modulus of the Ti–15Mo–5Zr–3Al alloy is ~ 84 GPa in the polycrystalline form [31], it can be lowered to approximately 44 GPa in a single crystal fabricated by the floating zone method when the crystal orientation is controlled to be <100> [32]. This value is considerably close to that of human bone (10–30 GPa [33]). Our group previously attempted to reduce Young's modulus by L-PBF via the development of crystallographic texture, and we achieved a reduction to ~ 69 GPa [22].

Here, pure Ti has a bcc structure at high temperatures (β-phase), but transforms into a hexagonal close-packed (hcp) structure at low temperatures (α-phase). Adding a sufficient amount of bcc-phase-stabilizing elements—such as Mo, Nb, and Ta—stabilizes the bcc structure, even at room temperature. However, it sometimes accompanies the formation of other phases, such as orthorhombic α″-phase, hexagonal ω-phase, and martensitic hexagonal α'-phase, depending on the alloy composition, temperature, cooling rate, etc. [28]. Generally, their formation in β-Ti increases its strength but accompanies a decrease in ductility [28]. Furthermore, the formation of the α-, α'-, α″-, and ω-phases increases the Young's modulus of the alloy [32,34]. As a result, their formation behavior must be controlled to consider its application as an implant material. For the Ti–15Mo–5Zr–3Al alloy, Mo was added as the bcc-phase-stabilizing element. Concerning the effect of Al addition on the microstructure of β-Ti alloys, Williams et al. first reported that Al addition strongly suppressed the precipitation of the ω-phase [35], which improved the ductility of β-Ti alloys. The addition of Zr in Ti–15Mo alloy was also reported to retard the precipitation of the ω-phase [36]. Considering this background, clarifying the effect of differences between L-PBF and EB-PBF on the variations in the microstructure is crucial.

In this study, we first established process maps to determine the appropriate fabrication conditions for each method in terms of densification and crystallographic texture evolution. We systematically studied the texture, microstructure, and mechanical properties of the Ti–15Mo–5Zr–3Al alloy fabricated by using EB-PBF and L-PBF to provide a fair and reliable comparison and a strategy to develop advanced materials with superior properties via AM.

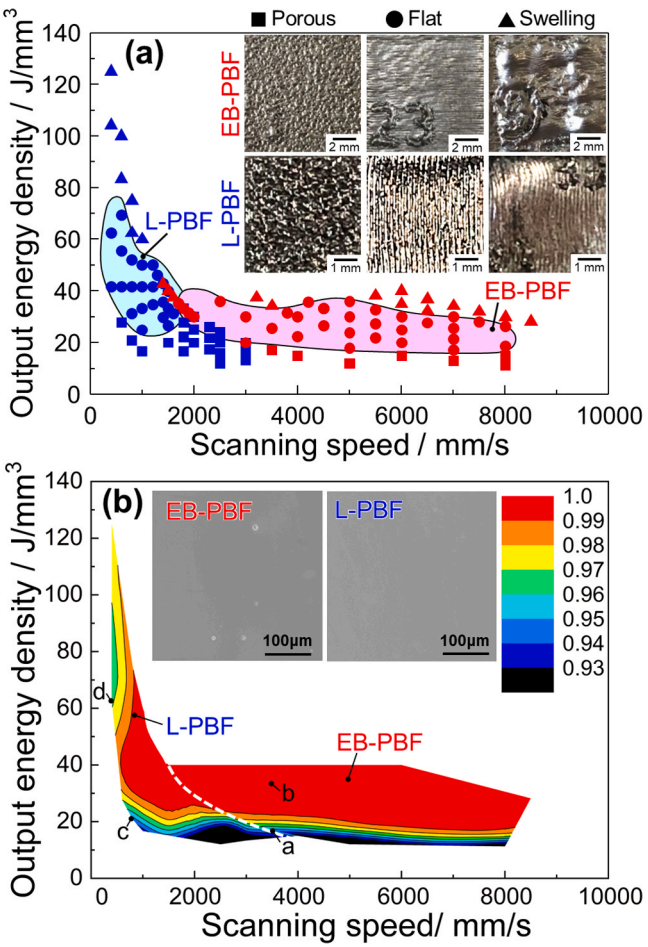

Fig. 2. Process map showing the (a) surface morphology and (b) relative density in EB-PBF and L-PBF. Insets in (a) show the typical top surface morphology with porous, flat, and swelling shapes in the EB-PBF- and L-PBF-built specimens, whereas those in (b) show the morphology of the pores in the EB-PBF- and L-PBF-built specimens selected for the tensile test. The colors in (b) represents the relative densities of the build part, with the red region indicating a relative density of the build part exceeding 99%. A white dashed line in (b) indicates the boundary of the L-PBF and EB-PBF areas. Note that the process conditions used in both L-PBF and EB-PBF coexist on the dashed line.

2. Methodology

2.1. EB-PBF and L-PBF process

The gas-atomized powders of the Ti–15Mo–5Zr–3Al alloy from the same production batch were used to compare the EB-PBF and L-PBF processes. Larger powders with particle sizes ranging from 44 μm (D_{10}) to 100 μm (D_{90}) (70 μm on average), were used in EB-PBF (Q10, Arcam, Sweden), whereas smaller powders, with particle sizes ranging from 18 μm (D_{10}) to 44 μm (D_{90}) (30 μm on average), were used in L-PBF (M290, EOS, Germany). Supplementary Table 2s lists the variations in the chemical compositions of the main elements in the Ti–15Mo–5Zr–3Al alloy before and after the EB-PBF and L-PBF processes.

The chemical compositions of the two types of raw powders are almost the same. The powders were spherical with several satellites, as

shown in Fig. 1(a) and (b). To identify the constituent phases, X-ray diffraction (XRD) pattern was recorded with a step size and time per step of 0.0084° and 29.8 s, respectively (Philips PW3040/60 X-pert Pro, PANalytical B.V., Netherlands). Cu-Kα radiation generated at a tube voltage and tube current of 45 kV and 40 mA, respectively, was used. The XRD analysis of the powder, as shown in Fig. 1(c), indicates that the constituent phases in the powder were a β-phase and a small amount of orthorhombic α″-phase martensite [37]. The α″-phase may have been caused by rapid cooling during the gas atomization process. The precise volume fraction of the α″-phase could not be evaluated, but the highest intensity of the α″-phase in the XRD profile was less than 1/8 of that of the β-phase. In the powder, the presence of a small amount of ω-phase is supposed, but detecting it in the conventional XRD analysis was difficult.

Cuboids with dimensions of 10 mm × 10 mm × 50 mm and 5 mm × 5 mm × 25 mm were fabricated by using EB-PBF and L-PBF, respectively, with their short edges parallel to the scanning directions and long edges parallel to the build direction. A smaller sample was prepared in L-PBF because the power and energy absorptivity of the laser beam are smaller than those of the electron beam. If the same cross-sectional size was used, the energy density of the laser beam would be much smaller than that of the electron beam at the same fabrication parameters. In this case, the available process window for high density and strong crystallographic texture would be quite narrow in L-PBF, which makes the comparison by using a similar microstructure difficult. Therefore, a smaller cross-sectional size was used in the L-PBF. The geometric size of the fabricated sample is indeed one of the factors that affect the fabrication conditions and the resultant microstructure. In this study, the mechanical properties of L-PBF- and EB-PBF-built specimens were examined in specimens with optimized textures and microstructures, by making the process map shown later in Figs. 2 and 4. This enabled a reasonable comparison of the mechanical properties of EB-PBF and L-PBF.

Supplementary Table 3s lists the main fabrication process parameters used in this study. Parameters, other than the beam power and scanning speed, were adjusted to the same values as possible to reduce the number of factors influencing the microstructure. The preheating temperatures for L-PBF and EB-PBF listed in Supplementary Table 3s indicate the initial temperature of the first layer. As the build height increases, the initial temperature of the build layer increases and approaches a stable value after a height by equilibrating the input and loss of heat, although the equilibrium temperature has not yet been experimentally determined.

In this study, the build direction was defined as the *z*-axis, and the scanning directions perpendicular to the *z*-axis were defined as the *x*- and *y*-axes. The scanning strategy was mainly bidirectional scanning with a 90° rotation in each layer, that is, an XY-scan. To clarify their texture formation mechanisms, some products were additionally prepared by using an X-scan without a 90° rotation in each layer.

2.2. Microstructure and mechanical property characterization

The cuboids were cut into two along the *yz*-plane in the center and then the *yz*-plane microstructure near the final upper layers of the built sample was analyzed using scanning electron microscopy (SEM) (JIB-4610F, JEOL, Japan) and transmission electron microscopy (TEM) (JEM-3010, JEOL, Japan). Before the SEM observations, the specimens were etched in a solution consisting of 2% HNO_3, 1% HF, and 97% H_2O for approximately 1 min with ultrasonic vibration at room temperature to clearly observe the melt-pool traces and grain boundaries. Thinning of the foil for TEM observation was conducted on a twin-jet machine (Tenupol-3, Struers, Denmark), with a solution consisting of 6% $HClO_4$, 35% butanol, and 59% methanol at approximately −25 °C. The relative density was obtained by calculating the average of the pore fraction in five SEM images captured at different positions of each specimen with mirror polishing using Image-Pro® Plus software to determine the tendency of the variation with different fabrication process parameters. The crystallographic textures developed in the specimens were examined by electron backscatter diffraction pattern analysis in the SEM, at a measured step size of 3 μm and an accelerating voltage of 20 kV. The software used for data collection and data processing were Aztec (Oxford Instruments, UK) and Channel 5 (Oxford Instruments, UK), respectively. We used the HKL tango in Channel 5 to clean up the inverse pole figure map by using the neighbors of 3 in the zero solutions of noise reduction windows.

The EB-PBF ($E = 36$ J/mm^3, $v = 5000$ mm/s) and L-PBF ($E = 50$ J/mm^3, $v = 1200$ mm/s) specimens with a relatively high density and strong texture were selected to compare the mechanical properties. Here, E and v indicate the output energy density and beam scanning speed in the AM process, respectively. Tensile specimens with a gauge of 5 mm length, 1.5 mm width, and 0.8 mm thickness were extracted near the final upper layers of the built sample. The loading direction and thickness direction were set parallel to the *z*- and *x*-axes, respectively. Tensile tests were performed on three specimens under each condition at room temperature, with a strain rate of 1.67×10^{-4} s^{-1}. To remove the influence of hydrogen embrittlement (if any), the tensile tests were conducted in a vacuum. The evaluation of nominal strain was evaluated by the displacement of the cross-head in the tensile apparatus, and the nominal stress was measured by a load cell.

2.3. Numerical simulation

From the experiment described in Section 2.2, the shape of the melt pool was suggested to be an important factor in controlling the texture evolution behavior, as described in detail later. A numerical simulation was conducted to confirm this and identify the factors that govern the shape of the melt pool. The 3D transient melt-pool model was developed using the commercial software COMSOL Multiphysics 5.2a (COMSOL Inc., USA). The width and length of the base material domain were 10 mm × 10 mm for the EB-PBF and 5 mm × 5 mm for the L-PBF. To improve the calculation efficiency, the height of the base material domains was only 1 mm for both EB-PBF and L-PBF. The dimensions of the domain of the powder were 10 mm × 10 mm × 0.05 mm for EB-PBF and 5 mm × 5 mm × 0.06 mm for L-PBF. One track in each layer was calculated. Fine and coarse meshes were used around the molten and surrounding regions, respectively. The heat transfer in the investigated model included heat absorption from the heat source, heat conduction in the powder and base material, heat dissipation through convection between the material boundary and chamber atmosphere, and heat radiation from the heated material.

The electron and laser beams are assumed to satisfy a Gaussian distribution, and their energy distributions in the three dimensions can be expressed as

$$Q = \frac{4\alpha P}{\pi R^2 H}\exp\left(-\frac{2r^2}{R^2}\right)\left(1-\frac{z}{H}\right) \qquad (0 < z < H), \tag{1}$$

in which α is the absorption coefficient of the beam, P is the output power of the beam, R is the radius of the beam, r is the distance from a point at the focus plane to the center of the beam, H is the influence depth of the beam with the maximum energy intensity, and z is the influence depth of the beam with arbitrary energy.

The heat conduction can be expressed by Fourier's equation [38].

$$\rho C_p \frac{\partial T}{\partial t} - k\Delta T = Q \tag{2}$$

Here, ρ is the effective density (kg/m^3), C_p is the heat capacity at constant pressure (J/(kg K)), T is the temperature (K), t is the time (s), k is the thermal conductivity (W/(m K)), and Q is the heat per volume obtained from the heat source (W/m^3).

The effective density is determined as

$$\rho = \rho_0(1 - \Phi), \tag{3}$$

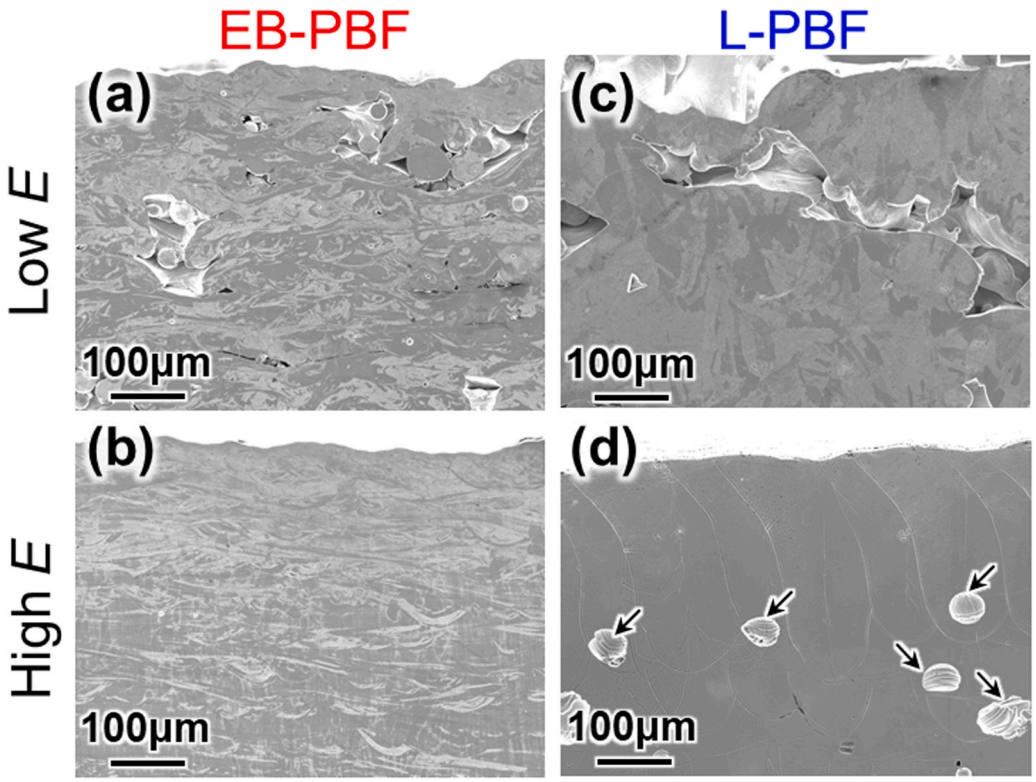

Fig. 3. Back scattered electron (BSE) images showing the morphology and position of the pores in the (a) and (b) EB-PBF-built specimens and (c) and (d) L-PBF-built specimens at (a) and (c) low and (b) and (d) high energy densities.

where ρ_0 is the solid density of the material and Φ is the porosity. Here, the porosity of the powder layer was considered to be 0.5, whereas at the bulk layer it was considered to be 0.

The thermal conductivity of the powder is defined as

$$k_{\text{powder}} = k_0(1 - \Phi) \tag{4}$$

in which k_{powder} and k_0 are the thermal conductivities of the powder and solid, respectively.

The heat loss by convection can be expressed as

$$Q_{\text{con}} = h(T - T_{\text{atm}}) \tag{5}$$

in which h is the coefficient of heat convection and T_{atm} is the atmospheric temperature, which was set to 25 °C. The heat loss by convection with air is neglected in EB-PBF because of its high vacuum (~ 0.1 Pa).

The heat loss by radiation can be expressed by the Stefan–Boltzmann law:

$$Q_{\text{rad}} = \varepsilon\sigma\left(T^4 - T_{\text{atm}}^4\right) \tag{6}$$

Here, ε is the material emissivity and σ is the Stefan–Boltzmann constant.

The initial temperature in the powder and base material regions at zero time was 80 °C for L-PBF and 520 °C for EB-PBF.

The natural boundary condition for the powder surface can be expressed as [39].

$$-k\frac{\partial T}{\partial n} = Q - Q_{\text{con}} - Q_{\text{rad}} \qquad (x, y, z) \in S, \tag{7}$$

where S represents the powder surface irradiated by the beam and n is the normal vector of surface S.

Supplementary Tables 4s and 5s list the physical properties of the Ti–15Mo–5Zr–3Al alloy [40] and the heat source parameters of L-PBF and EB-PBF used in the finite-element simulation, respectively.

3. Results

3.1. Comparison of process maps for surface morphology and relative density

To optimize the fabrication conditions, process maps of the surface morphology and relative density were studied first, as shown in Fig. 2. The surface morphologies of the specimens formed under different conditions were categorized as porous, flat, and swelling types and their variation with output energy density and scanning speed were investigated, as shown in Fig. 2(a). Here, the output energy density E is defined as

$$E = P/(vdt), \tag{8}$$

where P is the beam power (for EB-PBF, $P = UI$, U is voltage, and I is current), v is the scanning speed, d is the distance between the neighboring scanning tracks, and t is the layer thickness. The surface morphologies were classified by observing their appearance. A more quantitative consideration will be required in the future.

As shown in Fig. 2(a), as the output energy density increased, the surface morphology of the specimens tended to vary from a porous shape to flat and swelling shapes in both EB-PBF and L-PBF. Because using an electron beam with excessively high output energy largely melts the metal, the surface of the specimen is abnormally raised, which can damage the powder brush. In such a case, we terminated the experiment at an early stage of fabrication to protect the machine. Thus, we could not obtain a sample for evaluation for these high-energy EB-PBF regions. The surface morphologies varied between EB-PBF and L-PBF for fabrication with identical output energies and scanning speeds. Maintaining a flat specimen top surface is important for forming a stable and uniform powder bed and the subsequent production of dense parts. Fig. 2(a) shows that the fabrication condition window, which enables us to obtain a flat surface, is completely separated for EB-PBF (red background) and L-PBF (blue background) with respect to the scanning

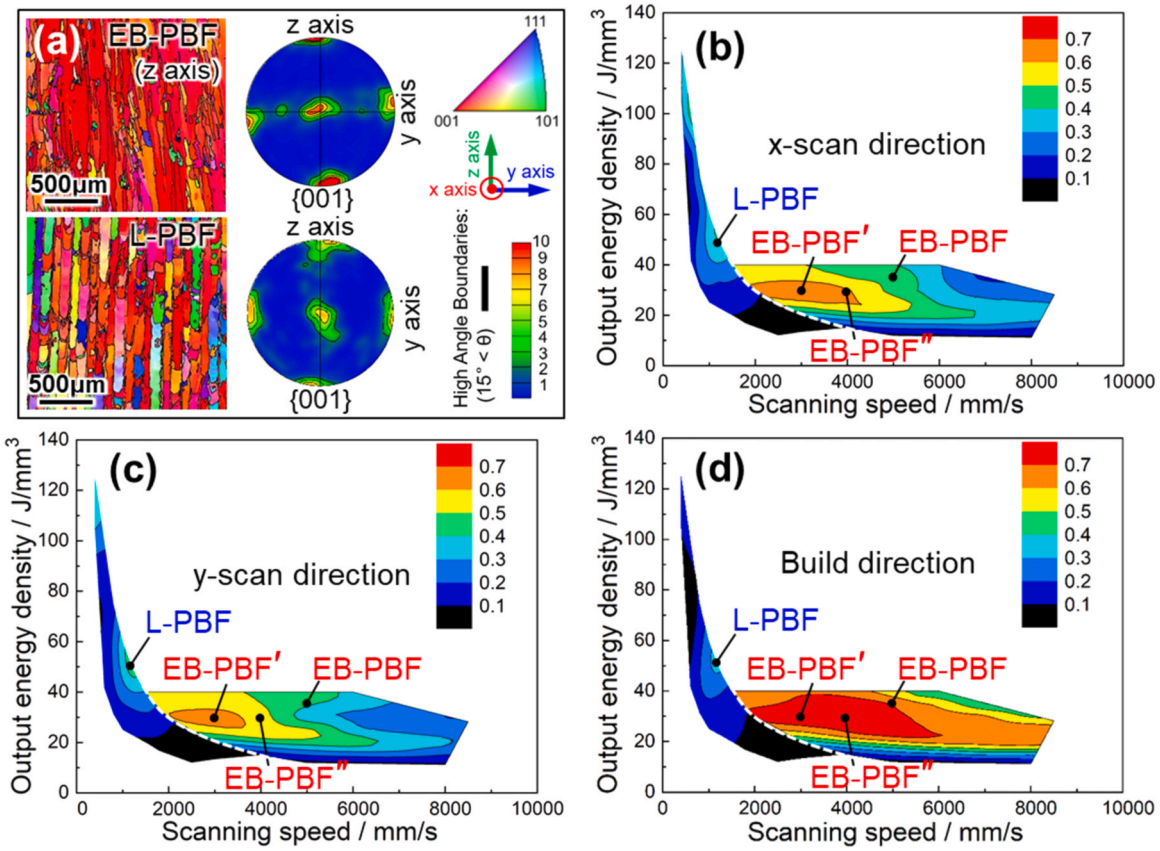

Fig. 4. (a) Crystallographic maps showing the single-crystal-like microstructure formed in the L-PBF- and EB-PBF-built specimens at the optimized conditions. The process map of <100> intensity in the (b) *x*-scanning direction, (c) *y*-scanning direction, and (d) build directions in EB-PBF and L-PBF. White dashed lines in (b)–(d) indicate the boundary of the L-PBF and EB-PBF areas. Note than the process conditions used in both L-PBF and EB-PBF coexist on the dashed line.

speed. This is believed to be primarily due to the difference in energy absorption activities (electron (0.9 [41]) and laser beams (0.7 [42]) for the Ti alloy) and preheating temperatures between EB-PBF and L-PBF (refer to Supplementary Table 1s).

Fig. 2(b) shows the variation in the relative density with the output energy density and scanning speed. At the same output energy density, the relative density increased as the scanning speed increased for both EB-PBF and L-PBF because a higher scanning speed reduces the time interval for melting between adjacent points in the adjacent scanning tracks, thus decreasing the thermal loss of the return point during the time interval. That is, the initial melting temperature increases at higher scanning speeds. However, when the scanning speed is considerably higher, the preheating effect from the adjacent track is insufficient to ensure the complete melting of the powder for the sharply reduced line energy density. Thus, the relative density decreases with the scanning speed at higher scanning speeds, particularly for L-PBF with a lower heat energy density. At the same scanning speed, the relative density generally increases with increasing output energy in the EB-PBF. However, as shown in Fig. 2(b), the tendency changed in L-PBF when the scanning speed was lower than 1000 mm/s, and the relative density decreased at higher output energy densities.

To elucidate this difference, the generation mechanism of the pores at different energy densities (marked by points a, b, c, and d in Fig. 2(b)) was investigated, as shown in Fig. 3. In both EB-PBF and L-PBF, lack-of-fusion-type defects were present in the specimens fabricated under the lower output energy, as shown in Fig. 3(a) and (c), because of the insufficient thermal energy supplied to the melt powders. With the higher output energy in EB-PBF shown in Fig. 3(b), the lack-of-fusion-type defects disappeared, and a dense specimen was obtained. However, numerous round pores—indicated by the black arrows in Fig. 3(d)—were observed at the bottom of the keyhole-shaped melt pools of the L-PBF-built specimens at a high energy density. The recoil pressure, which results from the collision between the evaporated gas and atmospheric gas, forms keyhole-type melt pools, and gas is entrapped during the collapse of the keyhole-type melt pools [10,43]. Thus, keyhole-type pores do not form in EB-PBF under vacuum, whereas they form in L-PBF under a gaseous (generally Ar or N_2) atmosphere. However, when the scanning speed was increased in L-PBF, pores were rarely observed at the bottom of the keyhole-type melt pool at the same high energy density, and dense specimens were obtained. This may be because the higher scanning speed makes the melt pool unstable by increasing the Rayleigh instability and/or Marangoni convection [44]. The keyhole-type melt pool collapsed before solidification. As a result, the gas was not easily entrapped in the solidified part.

3.2. Comparison of the crystallographic texture formation

Fig. 4(b)–(d) show the crystallographic texture process map with the output energy density and scanning speed along the *x*-, *y*-, and *z*-build directions in the XY-scan specimens, whereas Fig. 4(a) shows the typical crystal orientation maps. As described earlier in Section 2.2, the microstructure observation was conducted on the *yz*-plane; Fig. 4(a) indicates the crystal orientation color along the build direction as a representative example. In this study, the same expression method for the crystal orientation was used in the other crystal orientation maps, unless otherwise specified. Fig. 4(a) demonstrates that a cubic texture can be formed in both the EB-PBF- and L-PBF-built specimens under the optimized condition—that is, the <100> orientation is preferentially aligned parallel to the *x*-, *y* -, and *z*-directions. This feature is desirable for the development of noble implants because the alignment of the

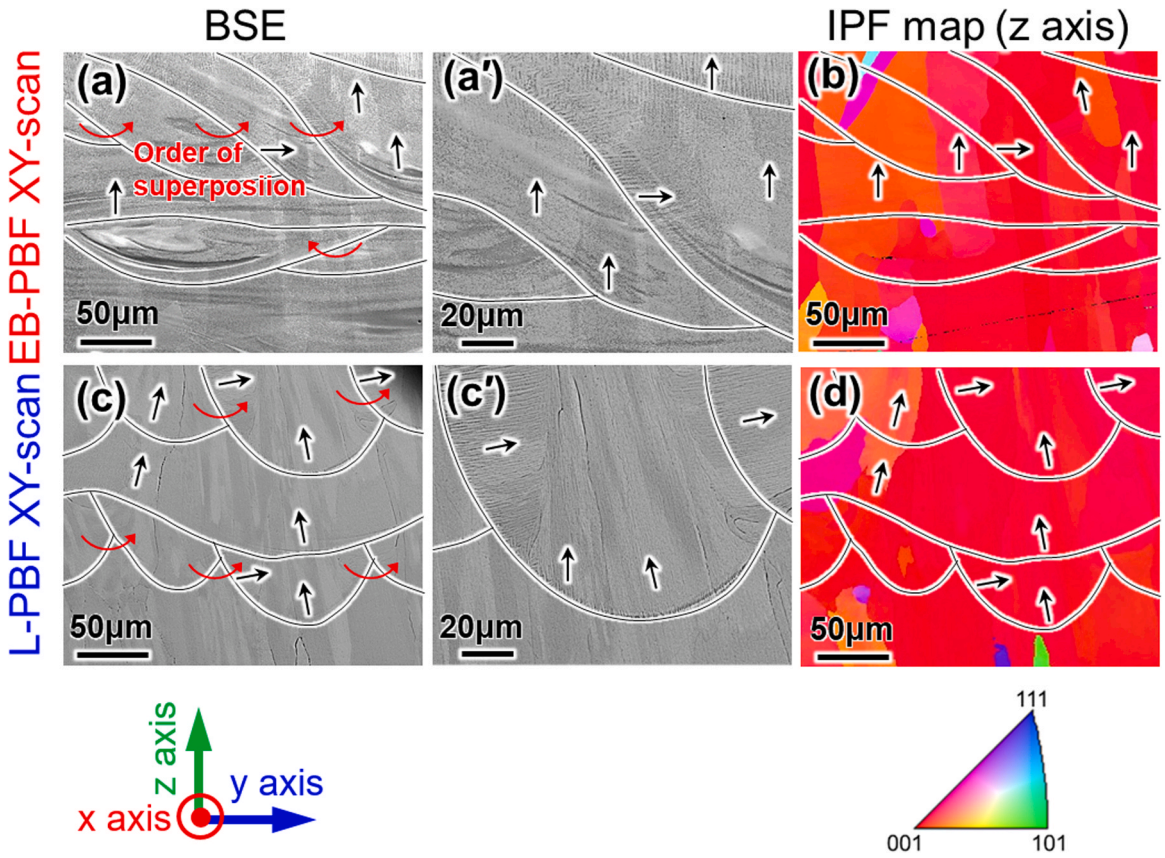

Fig. 5. BSE images showing the morphologies of the boundaries of the columnar cells and the traces of melt pools observed on the *yz*-plane in the (a) EB-PBF- and (c) L-PBF-built specimens. (a′) and (c′) Show higher magnification images of (a) and (c). (b) and (d) Show corresponding crystal orientation maps along the *z*-axis.

<100> orientation is important for inducing an extremely low Young's modulus [32], as described earlier in Section 1. The directionality of the <100> orientation was quantitatively evaluated, as shown in Fig. 4(b)–(d). In Fig. 4(b)–(d), the color in the map indicates the area fraction of the <100> grains along the measured direction, with a deviation of 15°. Fig. 4(b)–(d) also demonstrate that the single-crystalline-like microstructure in which <100> is aligned along all the *x*-, *y*-, and *z*-directions formed at a moderate energy density and scanning speed in L-PBF, whereas it was developed at a moderate energy density and low scanning speed in EB-PBF. Note that the texture intensity in the EB-PBF-built specimen was considerably higher than that in the L-PBF-built specimen in the *x*-, *y* -, and *z*-directions.

To clarify the origin of the difference in texture intensity, further microstructural observations were performed. Fig. 5(a) and (c) show the SEM images of the EB-PBF- and L-PBF-built specimens, the morphologies of the grain boundaries, and the traces of melt pools examined by etching and their enlarged images. Fig. 5(b) and (d) show the corresponding crystal orientation map along the *z*-axis (build direction). Note that the observation was conducted at the top layer of the built product to examine the shape of the melt pool without the influence of subsequent repetitive heating, which is a distinctive feature of layer-by-layer fabrication. The alternative half ellipses and the bands along the *y*-axis in Fig. 5(a) and (c) were identified as the melt-pool traces along the *x*- and *y*-scanning directions, respectively. The superimposed sequence (red arrows) for the melt pools in the same layer was always from right to left in the *x*-scanning in L-PBF, whereas it alternated in each *x*-scanning in EB-PBF. These fixed characteristics depend on the operating machine. This suggests that the entire temperature distribution in the EB-PBF-built specimen may be much more uniform than that in the L-PBF-built specimen.

In Fig. 5(a) and (c), black arrows indicate the elongated directions of the columnar cells. In the melt pools in both the EB-PBF- and L-PBF-built specimens, the majority of the columnar cells tended to grow along the build direction and traversed the melt-pool boundaries. However, some columnar cells were found to grow horizontally on the side of the melt pools of the L-PBF-built specimen; in contrast, they were occasionally found only in the EB-PBF-built specimen. By comparing the cellular-type microstructure in Fig. 5(a) and (c) and their corresponding crystal orientation maps in Fig. 5(b) and (d), it was found that the elongated direction of columnar cells almost corresponded to <100>, and both the vertically and horizontally aligned columnar cells contributed to the development of the <100> texture along the build direction. That is, although the same textures were formed in the EB-PBF- and L-PBF-built specimens, the columnar cells constituting the texture were aligned differently which indicates that the texture development processes vary in EB-PBF and L-PBF, resulting in different texture intensities.

To elucidate the differences in the texture development mechanism more clearly, the specimen was fabricated using an X-scan strategy. Fig. 6 shows the typical crystallographic textures developed in the X-scan specimens, and Fig. 7 shows the captured SEM images and crystal orientation maps at the same position of the *yz*- and *xz*-planes. In the case of EB-PBF, the <100> orientation in Fig. 6(a) aligned preferentially along the build direction in the X-scan, and the same cubic texture, shown in Fig. 6(b), as that observed in the XY-scan specimen, shown in Fig. 4(a) was developed. However, in the case of L-PBF, the <110> orientation (Fig. 6(c)) aligned preferentially along the building direction in the X-scan, as reported previously [22]. This is different from the <100> orientation in the XY-scan; the cubic texture shown in Fig. 6(d) rotated by 45° along the *x*-scanning direction, compared with the one developed in the XY-scan. That means that different textures developed in the X-scan between the EB-PBF and L-PBF.

Fig. 7 shows that the columnar cells existed primarily on the plane

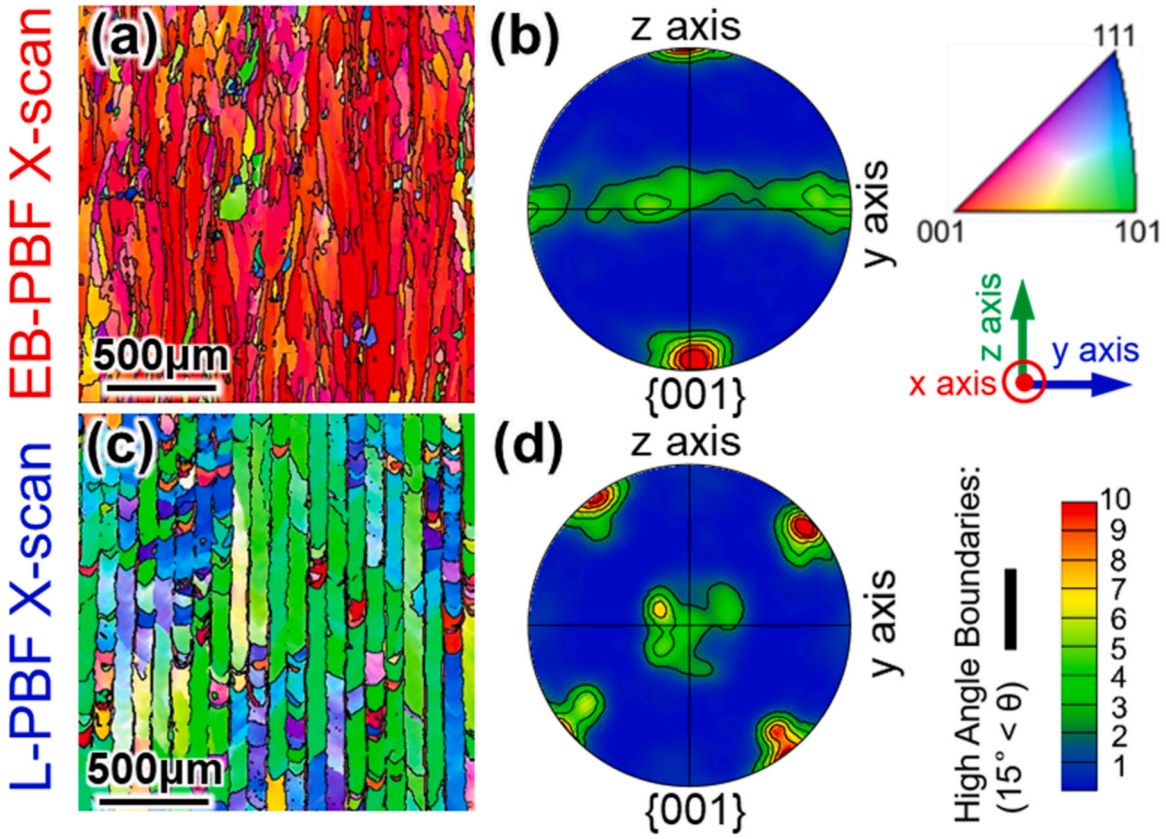

Fig. 6. (a) and (c) The crystal orientation maps and (b) and (d) pole figure maps show the crystallographic textures developed in the (a) and (b) EB-PBF-built specimens and (c) and (d) L-PBF-built specimens with X-scan.

perpendicular to the scanning direction in both the EB-PBF- and L-PBF-built specimens with X-scan, that could be confirmed by the observation on the *xz*-plane shown in Fig. 7(c) and (d). The superimposed sequence (red arrows) for the melt pools in the adjacent layers was the same in EB-PBF and L-PBF with X-scan, indicating a similar temperature variation in their specimens. A comparison of the cellular-type microstructure and its corresponding crystal orientation map, as shown in Fig. 7(a)–(d), indicates that the vertically aligned columnar cells (indicated by the black arrows) contribute to the development of the <100> texture along the build direction in EB-PBF, whereas those inclined from the build direction by ± 45° contributed to the development of the <110> texture along the build direction in L-PBF. The reason for the different variations in texture with the scanning strategy for EB-PBF and L-PBF is discussed in Section 4.1.

3.3. Comparison of the secondary phase formation

Because of the significant difference in the thermal history of EB-PBF and L-PBF, the secondary phase formation in the EB-PBF- and L-PBF-built specimens was compared. Fig. 8(a) and (b) show typical back-scatter electron (BSE) images of the EB-PBF- and L-PBF-built specimens, which were captured near the final upper layers of the built sample. Plate-like precipitates could be widely observed, concentrated at the columnar cell boundaries and in the vicinity of some melt-pool boundaries (indicated by the green arrow) in the EB-PBF-built specimen; however, they were not found in the L-PBF-built specimen. By comparing the XRD results in Fig. 8(c) of the EB-PBF- and L-PBF-built specimens and the raw powders, additional diffraction peaks were found in the EB-PBF-built specimen, which were believed to be from the plate-like precipitates shown in Fig. 8(a). The diffraction peaks indicate that the precipitate was the α-phase.

TEM observations were conducted to further confirm the presence of precipitates. Fig. 9(a), (c) and (e) show the dark field images (DFIs) of the EB-PBF- and L-PBF-built specimens, respectively. Fig. 9(b), (d), and (f) show the corresponding selected area electron diffraction (SAED) patterns. Fig. 9(a)–(f) are observed in the beam directions (BDs) parallel to the $[11\bar{1}]$ and $[\bar{1}10]$ directions of the β-matrix with the bcc structure. The green circles in Fig. 9(b), (d), and (f) indicate the diffraction spots used to obtain the DFIs. In the diffraction pattern shown in Fig. 9(b), (d), and (f), numerous diffraction spots or streaks can be observed in addition to those from the β-matrix, which supposedly originate from either the α-, ω-, or α″-phases, which have an orientation relationship with the β-matrix as follows [45,46]:

$$\alpha-\text{phase}: \ (0001)_{\alpha}\,//\,\{1\bar{1}0\}_{\beta}, \quad <11\bar{2}0>_{\alpha}\,//\,<111>_{\beta} \tag{9}$$

$$\omega-\text{phase}: \ (0001)_{\omega}\,//\,\{111\}_{\beta}, \quad <11\bar{2}0>_{\omega}\,//\,<1\bar{1}0>_{\beta} \tag{10}$$

$$\begin{aligned}\alpha'-\text{phase}: \ &\{110\}_{\alpha''}\,//\,\{2\bar{1}1\}_{\beta}, \quad <001>_{\alpha''}\,//\,<0\bar{1}\bar{1}>_{\beta}\\ &\{020\}_{\alpha''}\,//\,\{0\bar{1}1\}_{\beta}, \quad <100>_{\alpha''}\,//\,<100>_{\beta}\end{aligned} \tag{11}$$

Fig. 9(a) clearly shows that the additional diffraction spots in Fig. 9(b) are from the plate-like α-phase. However, no precipitates can be observed in Fig. 9(c) and (e) using the diffraction spots $\{\bar{1}010\}$ of the ω-phase indicated by the green circle in Fig. 9(d) and (f) because the ω-phase exists only in microclusters, which are quite small for observation. This can be inferred from the streak patterns shown in Fig. 9(d) and (f). This observation result is in good agreement with a previous study that used a single crystal, where the addition of Al to the Ti–15Mo–5Zr alloy strongly hindered the precipitation of both athermal and isothermal ω-phases [29]. However, the intensity of the streak pattern in EB-PBF is slightly stronger than that in L-PBF, as shown in

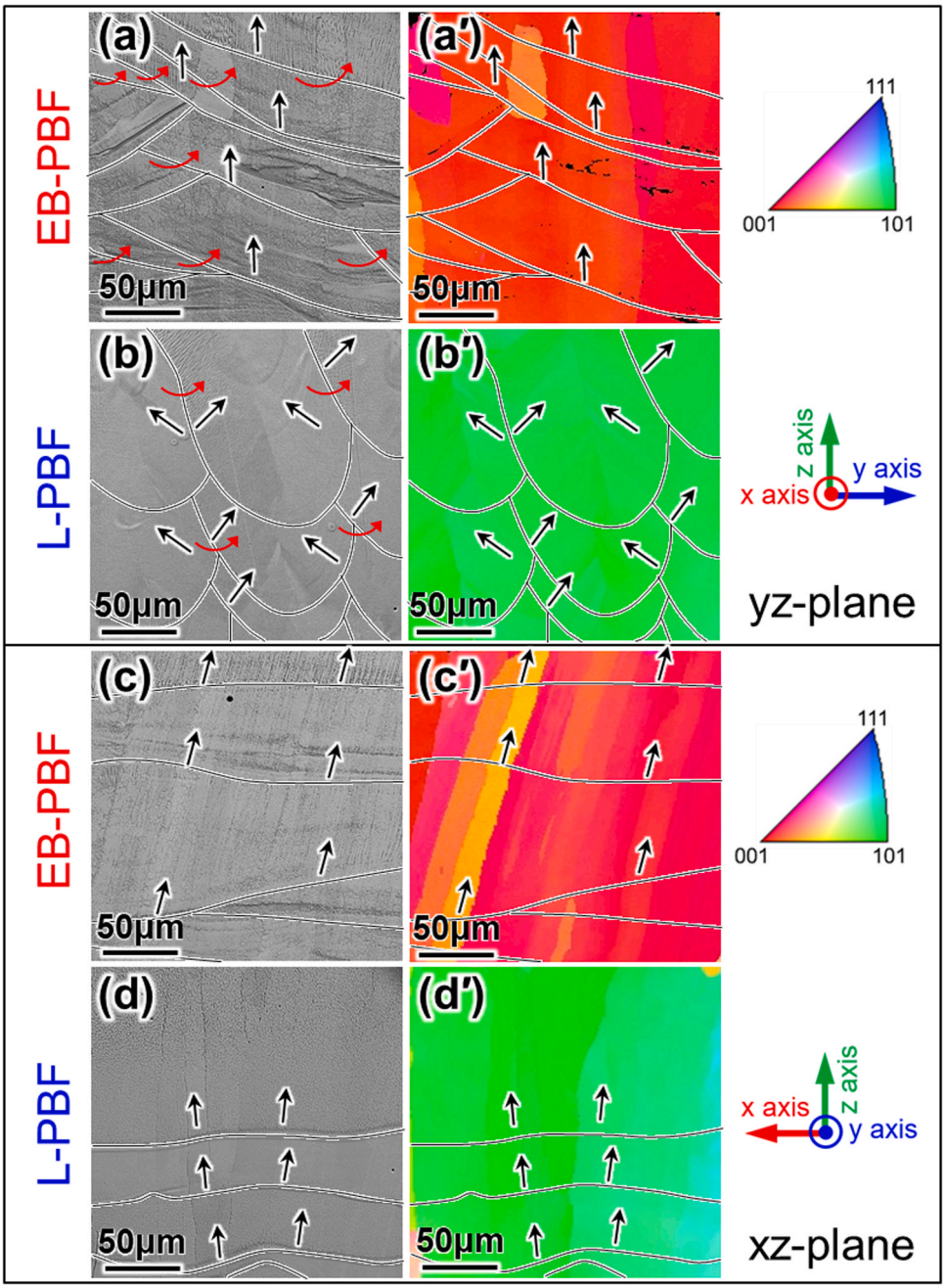

Fig. 7. (a–d) BSE images and their corresponding (a′–d′) crystal maps at the same position showing the columnar cell growth in the melt pools of the (a), (a′), (c), and (c′) EB-PBF- and (b), (b′), (d), and (d′) L-PBF-built specimens with X-scan. (a), (a′), (b), and (b′) *yz*-plane, (c), (c′), (d), and (d′) *xz*-plane.

Fig. 9(d) and (f). This indicates that the size of the ω-phase microcluster may increase in EB-PBF because of the preheating effect.

Fig. 10 shows the additional TEM analysis results of the EB-PBF- and L-PBF-built specimens. Many fringe patterns were observed in the grains of the EB-PBF- and L-PBF-built specimens, as shown in Fig. 10(a), (d), and (e). The observed microstructure is considerably similar to those observed in β Ti-Nb alloys fabricated by EB-PBF [47] and L-PBF [48], in which the fringe patterns were attributed to lamellar-like α″-martensite. The observed frequency of the fringe patterns was significantly higher in the L-PBF specimen than in the EB-PBF specimen. In addition, a jagged boundary was observed in the L-PBF-built specimen, as shown in Fig. 10 (d), implying that twinning or martensitic transformation may occur in the L-PBF-built specimen. In the grains labeled A, B, and C in Fig. 10(d), the same diffraction pattern as that in Fig. 10(g) was observed, indicating that twinning does not exist in the L-PBF-built specimen. Therefore, α″-martensite formation in the grains may be the reason for the formation of the jagged boundary observed in Fig. 10(d).

Here, the fringe patterns in the bright field images (BFIs) can be made invisible (Fig. 10(b) and (f)) by selecting the operation vectors (**g**) that are nearly parallel to them. This indicates that the fringe patterns in BFIs should not originate from the thick lamellar α″, but instead from a series of thin stacking fault-like α″-phases parallel to the observation direction. According to the invisibility criterion of $\mathbf{g}\cdot\mathbf{R} = 0$ or integer (in which **R** is the displacement vector), the displacement vector of stacking faults is supposed to be vertical to the plane in which the stacking faults lie, although further details have not yet been clarified. The thin stacking fault-like α″-phase has never been observed in the cast or floating zone-fabricated Ti–15Mo–5Zr–3Al alloys [29,32], and no significant variation in the main chemical composition of the Ti–15Mo–5Zr–3Al alloy was found before or after the EB-PBF and L-PBF

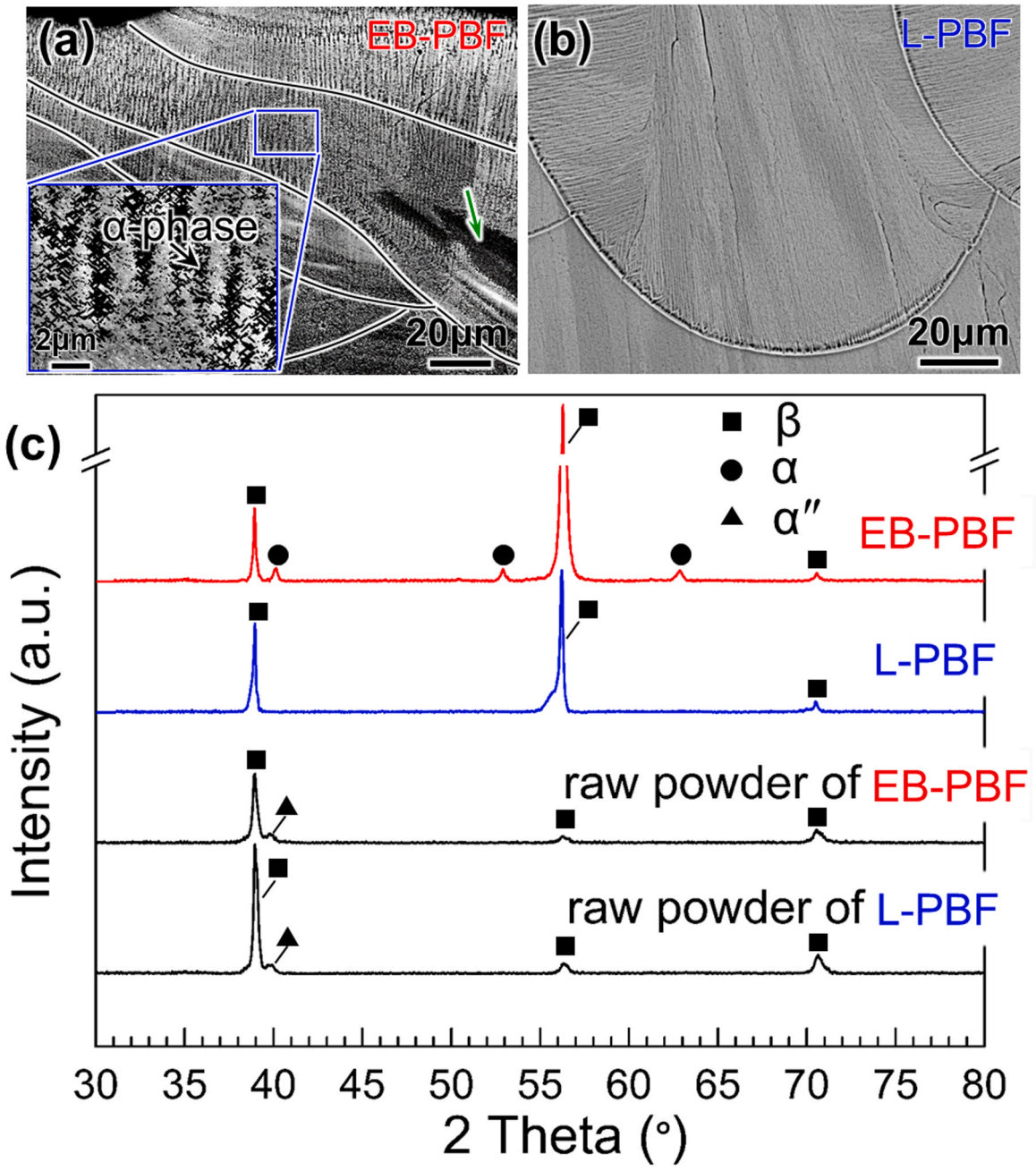

Fig. 8. BSE images of the (a) EB-PBF- and (b) L-PBF-built specimens. (c) Comparison of the X-ray diffraction profiles of the raw powders and EB-PBF- and L-PBF-built specimens.

processes, as shown in Supplementary Table 2s. This indicates that the formation of the stacking fault-like α″-phase in the AM-fabricated Ti–15Mo–5Zr–3Al alloy relates to the unique characteristic of AM, which is the repeated heating and cooling cycles. Although the β-phase in Ti–15Mo–5Zr–3Al alloy is stable and does not transform into the α″-phase during deformation [29], repeated heating and cooling cycles can generate a complicated thermal stress field [49], which might induce the $\{0\bar{1}1\}<011>$ shuffle in the β crystal lattice to form a layer of atomic arrangement of α″ [50]. The detailed formation mechanism of the stacking fault-like α″-phase will be studied in the future.

3.4. Comparison of the tensile property

Fig. 11 shows the typical stress-strain curves and fracture surfaces of the EB-PBF- and L-PBF-built specimens, with high relative density and strong texture intensity (in the build direction). The EB-PBF-built specimen with a stronger cubic texture—labeled as EB-PBF' and EB-PBF″ in Fig. 4(b)–(d)—was not selected for comparison because it exhibited a somewhat poor ductility because of the crack, which could not be observed before etching, as shown in Supplementary Figs. 1s and 2s. The reason for the formation of cracks in these specimens has not yet been clarified, and further studies are required.

Fig. 11(a) shows that the L-PBF-built specimen exhibited a considerably higher ductility but a slightly lower strength than the EB-PBF specimen. Supplementary Table 6s lists the 0.2% yield stress, ultimate tensile stress, and elongation. Although the L-PBF-built specimen has no α-phase, it has much more stacking fault-like α″-phase present than in the EB-PBF-built specimen, as confirmed by the density of fringe patterns in Fig. 10(a), (d), and (e). Because the α″-phase can significantly strengthen β-Ti [47,51], it can compensate for the absence of a

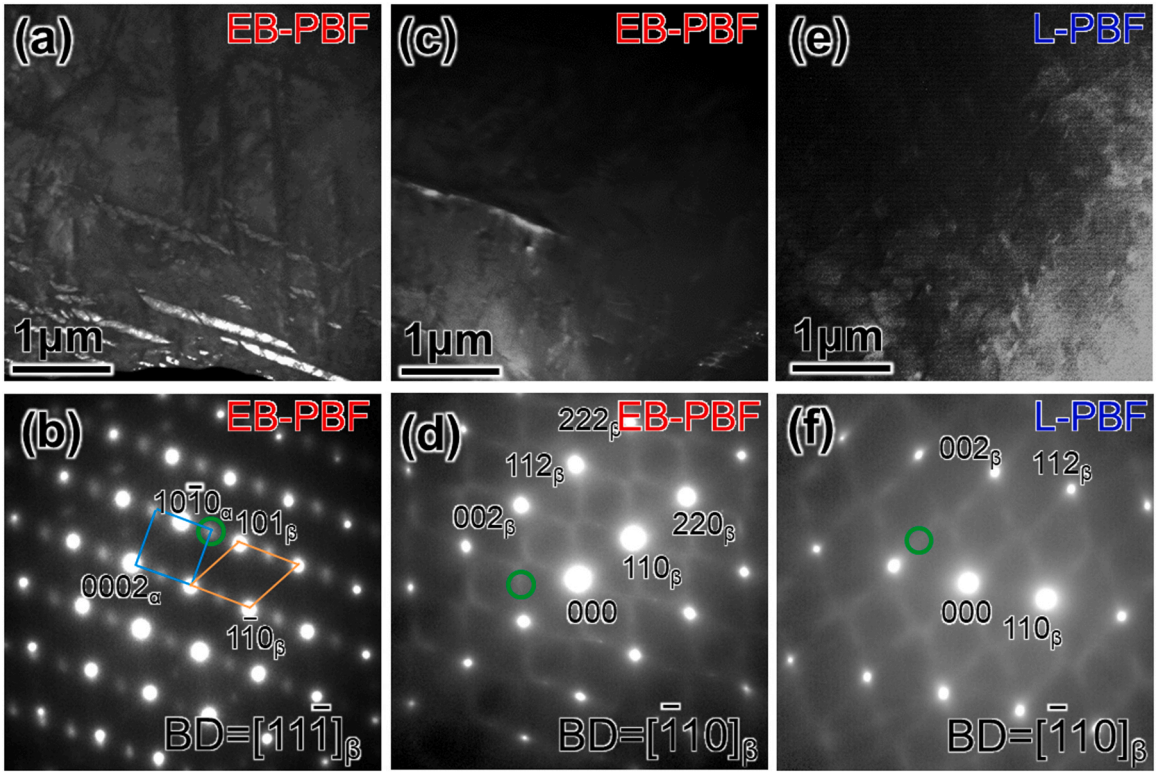

Fig. 9. TEM DFIs of (a) and (c) EB-PBF- and (e) L-PBF-built specimens. Corresponding SAED patterns observed parallel to (b) $[11\bar{1}]$ and (d) and (f) $[\bar{1}10]$ of β-Ti, respectively. The green circles in (b), (d), and (f) indicate diffraction spots used to take the DFIs.

strengthening effect from the α phase for the L-PBF-built specimen, making the strength of the L-PBF-built specimen only slightly lower than that of the EB-PBF-built specimen. Fig. 11(b)–(e) show the fracture surfaces of the specimens. The formation of dimple patterns was consistent with their ductility. In addition, some round pits were observed in the EB-PBF-built specimen, which were believed to be from the detached unmelted/incompletely melted powders that formed accidentally. Because the EB-PBF-built specimen shows good ductility (~ 15% elongation), the unmelted/incompletely melted powders should not be the main factor causing the ductility difference between the EB-PBF- and L-PBF-built specimens. Fig. 8 shows that the main difference in the microstructures of the EB-PBF- and L-PBF-specimens is the presence of an α-phase. Therefore, the existence of the α-phase in the EB-PBF-built specimens is the main reason for its poor ductility, compared with the L-PBF-built specimens under the condition of strong texture intensity and high relative density.

Fig. 12 shows the TEM images of the EB-PBF- and L-PBF-built specimens after deformation, with the BD parallel to the $[\bar{1}10]$ direction of the β-Ti matrix. Straight line-like contrasts were abundantly observed in the BFIs, which were confirmed to be dislocations with the Burgers vector parallel to <111> by the invisibility criterion of $\mathbf{g}\cdot\mathbf{b} = 0$. Twinning or martensitic transformations were not observed. That is, the operative deformation mode of the EB-PBF- and L-PBF-built specimens is <111> dislocation slip, which is the same as that of the floating zone-fabricated specimen [29]. This indicates that the deformation mechanism of the EB-PBF- and L-PBF-built specimens does not vary because of the unique stacking fault-like α″-phase, which may be because of the relatively high stability of the β-phase in the investigated alloy. Note that the dislocations are often tangled in the local region, as indicated by the red arrow in Fig. 12(b), and intersecting with a stacking fault-like α″-phase, as indicated by the green arrow in Fig. 12(b). This indicates that, although the existence of a stacking fault-like α″-phase does not alter the deformation mode, it prevents dislocation slip and increases the strength of the alloy. Although the precipitation of α-, α″-, and ω-phases is considered to affect the Young's modulus, as well as the strength and ductility, a comparison of Young's modulus in L-PBF and EB-PBF specimens has not yet been conducted. Thus, further studies to clarify the variations in mechanical properties and microstructure depending on the fabrication conditions are important for further development of this AM-prepared alloy.

4. Discussion

4.1. Effect of the melt-pool shape on texture formation

This study found that two different crystallographic orientations, <100> and <110>, were developed in the build direction of EB-PBF and L-PBF at the same X-scan, respectively. In our previous study, the formation of the <110> texture using the X-scan in L-PBF was found, and its formation mechanism was discussed in detail [22,25]. In contrast, the evolution of the <100> texture in the EB-PBF is unique. The formation mechanism and the reason why different textures, compared to those in L-PBF, have evolved are significantly interesting topics.

To clarify their physical origin, we focused on the expectation that the melt-pool shape should vary between the EB-PBF- and L-PBF-built specimens. The difference in the melt-pool shape significantly varies the temperature gradient direction and affects the columnar cell growth; this must be related to the different crystallographic texture developments in EB-PBF and L-PBF at the X-scan. To clarify this, the solidification behavior of the melt pool was investigated in detail.

Fig. 13(a) and (b) show the melt-pool shape of the EB-PBF- and L-PBF-built specimens in which a strong texture developed. The melt pools were shallow and wide in EB-PBF, but deep and narrow in L-PBF. The width and depth were 456 ± 54 μm and 87 ± 9 μm, respectively, in the EB-PBF and 312 ± 21 μm and 289 ± 10 μm, respectively, in the L-PBF. Fig. 13(c) and (d) show the simulation results of the melt-pool boundaries on the *yz*-plane in the EB-PBF- and L-PBF-built specimens at the

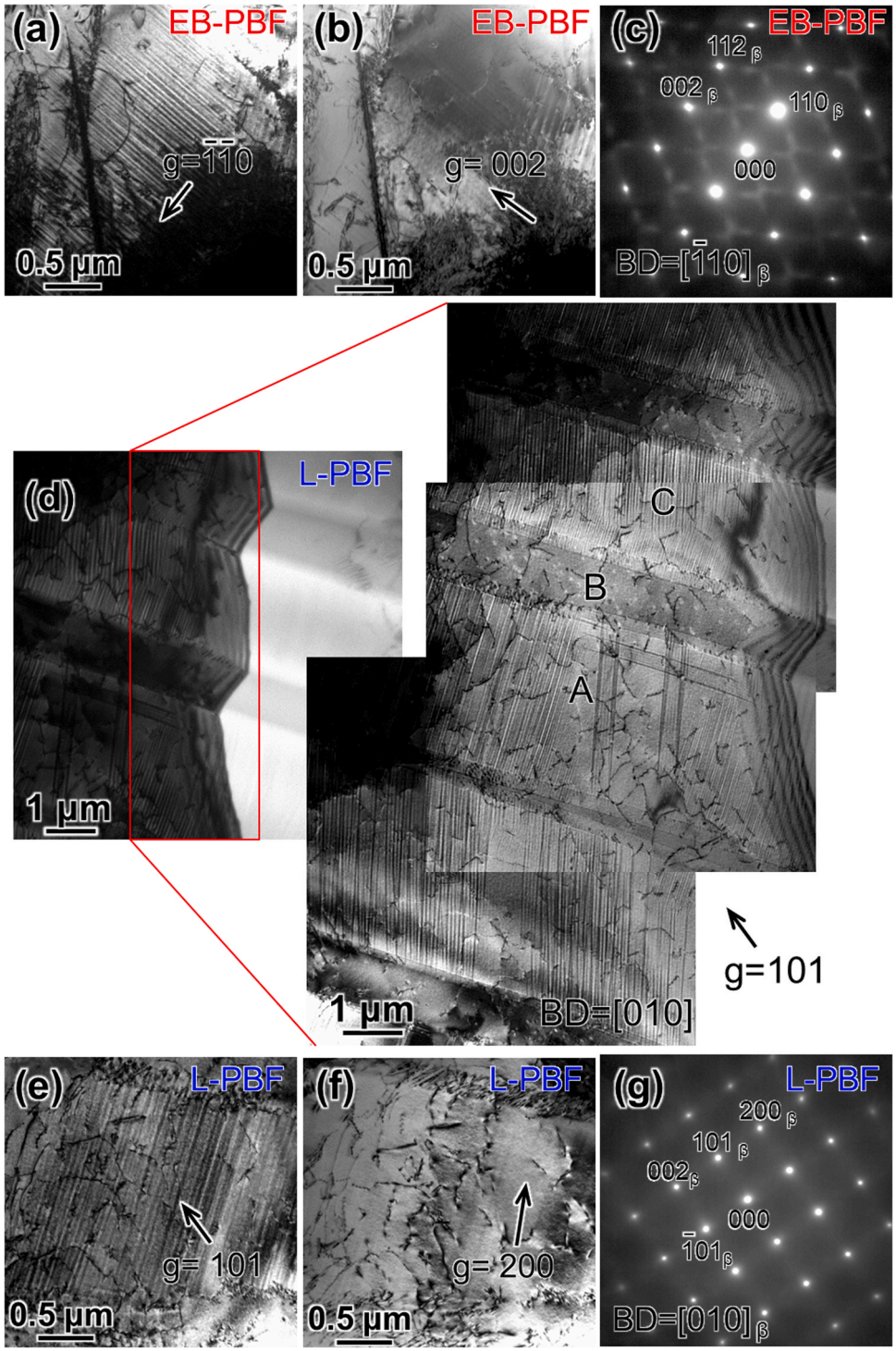

Fig. 10. TEM BFIs showing the stacking fault-like α″-phase in the (a) and (b) EB-PBF-built specimens and (d), (e), and (f) L-PBF-built specimens. Corresponding SAED patterns observed parallel to (c) [$\bar{1}$10] and (g) [010] of β-Ti.

center of the scan track at different times. When the beam passed through the investigated position in the EB-PBF, the depth of the melt pool increased, whereas the width of the melt pool decreased before the entire melt pool began to decrease. However, in the case of L-PBF, the depth of the melt pool first increased and then decreased, whereas the width of the melt pool continued to increase. This indicates that the observed melt-pool traces in the experiment corresponded to the ultimate migration position of the melt pools—that is, the initial solidification position—and solidification does not initiate on the observed melt-pool traces simultaneously. The solidification of the melt pool in EB-PBF first proceeds from the side to the center and then from the bottom to the top; however, that in L-PBF always proceeds from the bottom to the top. Although the melt-pool size has some differences, the ultimate migration position of the melt pool in the simulation agrees with the observed melt-pool traces.

Fig. 14(a) and (b) show the angle variation in the temperature gradient direction at the initial solidification position of the melt pool relative to (a) the *yz*-plane (that is, the plane perpendicular to the

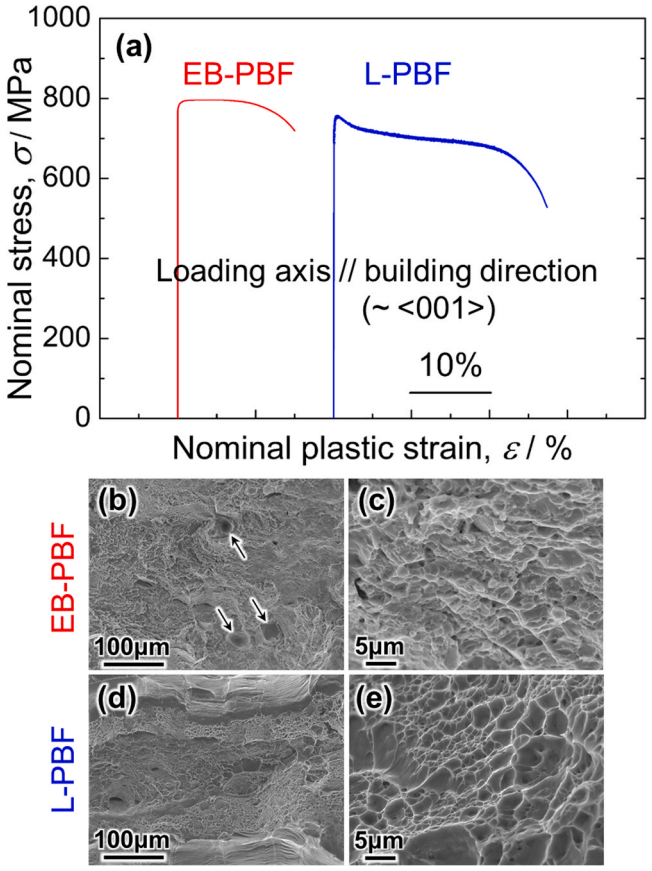

Fig. 11. (a) Tensile stress and strain curves and fracture surface of (b) and (c) EB-PBF-built specimens and (d) and (e) L-PBF-built specimens under the conditions of stronger crystallographic texture and higher relative density.

scanning direction) and (b) the build direction in the center of the scan track of EB-PBF and L-PBF, respectively. Here, the horizontal axis indicates the "relative" depth (position along the depth direction divided by the maximum depth in the melt pool from bottom to top), and only the angle on the right side of the melt pool was considered because of the melt-pool symmetry. Fig. 14(a) shows that the angle between the temperature gradient direction and the *yz*-plane was less than 3° throughout the depth in EB-PBF and L-PBF, except for the part adjacent to the bottom in L-PBF. This implies that the temperature gradient direction during solidification nearly exists on the plane perpendicular to the scanning direction. Therefore, the growth of the columnar cells in EB-PBF and L-PBF tends to occur on the plane perpendicular to the scanning direction when a strong texture is developed, although their melt-pool shapes are considerably different. However, with respect to the angle between the temperature gradient direction and the build direction shown in Fig. 14(b), it was less than 30° throughout the depth in EB-PBF, whereas in L-PBF, it largely varied depending on the position in the range of 30–75°. This indicates that the effect of the temperature gradient direction causes the columnar cells in the melt pools to grow toward the build direction in EB-PBF, but largely away from the build direction in L-PBF.

However, epitaxial growth affects the growth direction of columnar cells with respect to the underlying cells, which decreases the nucleation energy. We previously clarified that such epitaxial growth can occur when the angle between the temperature gradient direction and the epitaxial direction is less than 45° [20,23] in L-PBF specimens. In the case of EB-PBF, in any layer, most columnar cells beneath the melt pool are in the center of the melt pool in the last track because the melt pool is wide, as shown earlier in Fig. 13(a). The elongated direction of these columnar cells was parallel to the temperature gradient direction (that is, along the build direction). Then, the angle between the temperature gradient direction and the epitaxial direction equals the angle between the temperature gradient direction and the build direction (less than 30°), as shown in Fig. 14(a). Therefore, the columnar cells tend to grow along the build direction after the track-by-track process in one layer.

In the X-scan of EB-PBF, the above process is repeated in subsequent layers, thus forming vertically aligned columnar cells. Because the extending directions of the columnar cells are parallel to <100>, the <100> texture develops in the build direction in the X-scan of EB-PBF, in contrast to L-PBF.

Conversely, in the case of L-PBF, the columnar cells beneath the melt pool are on the side of the melt pool in the last track in any layer because the melt pool is narrow, as shown in Fig. 13(b). The elongated direction of these columnar cells should deviate from the build direction by approximately 30–75° if they are controlled by the temperature gradient direction. However, in reality, the cell growth direction is stabilized at 45° and −45° with respect to the build direction in the left and right halves of the melt pool, respectively, as shown in Fig. 7(b) and (b′). The inclined ± 45° angle of the columnar cells is considered advantageous for reducing the interfacial energy at the center of the melt pool, where the solidification front of the right and left parts is encountered. Therefore, the orientation perpendicular to the scanning direction is adjusted as the crystallographic misorientation in the right and left halves of the melt pool decreases, leading to a ± 45° cell growth from the build direction, thus forming the <110> texture in the build

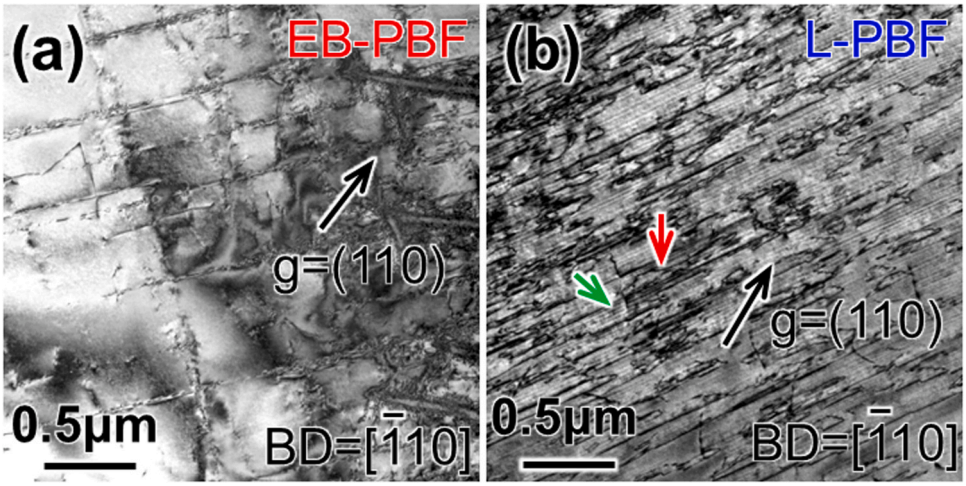

Fig. 12. TEM BFIs showing the dislocations in the (a) EB-PBF- and (b) L-PBF-built specimens after the tensile test.

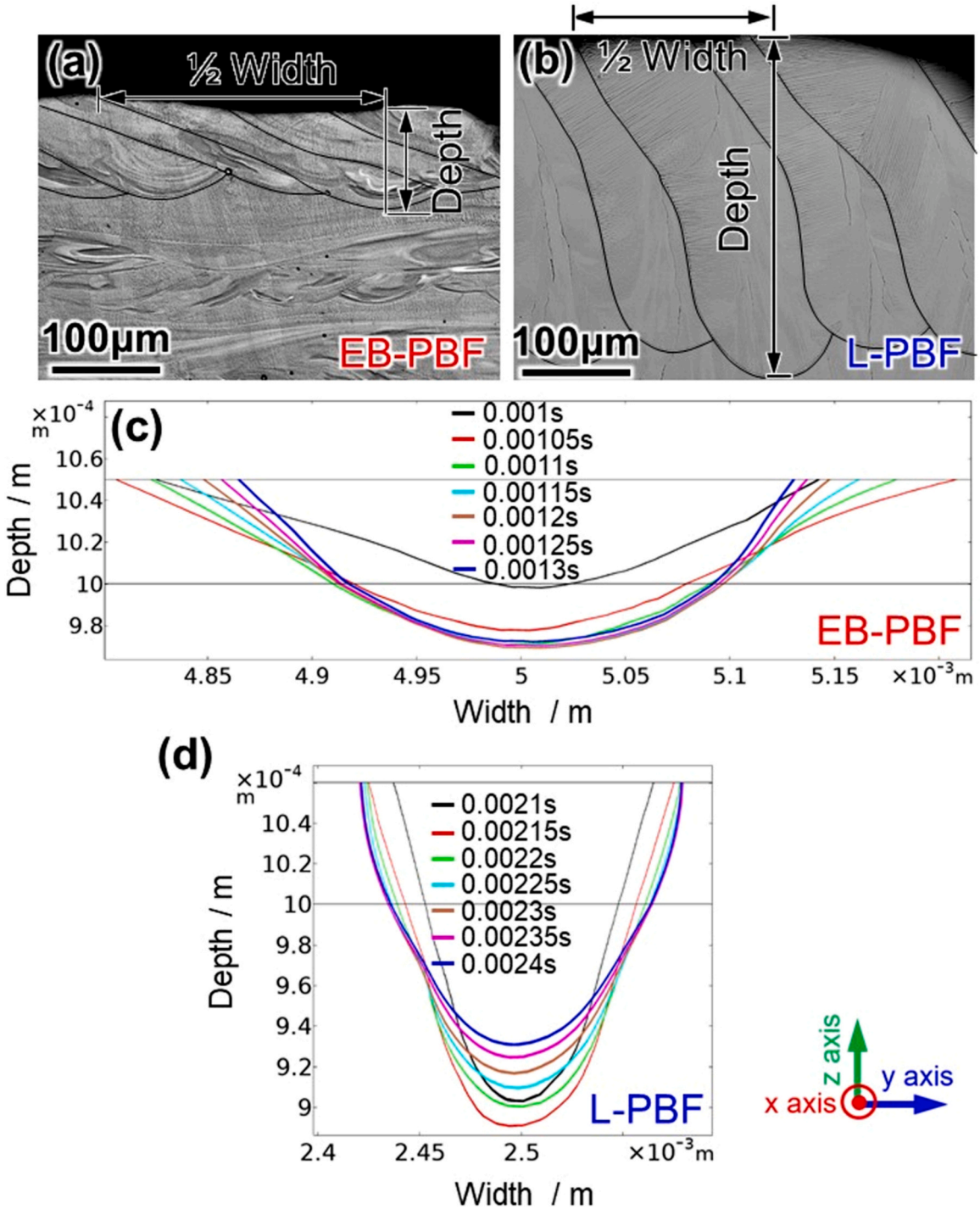

Fig. 13. BSE images showing the melt-pool morphologies of the (a) EB-PBF and (b) L-PBF-built specimens. Simulation results showing the migrations of the melt-pool boundaries on the *yz*-plane in the (c) EB-PBF- and (d) L-PBF-built specimens at the center of the scan track at different times.

direction, as explained in previous papers [22,25].

Because the laser scan in the X direction and that in the Y direction generate a melt pool with essentially identical shapes and sizes, the simulation results of the melt pool morphology and thermal gradient angle shown in Figs. 13 and 14 can be applied to both X- and XY-scan strategies. However, because the laser scanning direction is orthogonal between layers in the XY-scan, considering the combination of the thermal gradient angle and the associated cell growth direction between layers is necessary to discuss the crystallographic texture evolution behavior. The differences in the melt-pool shape affect the evolution mechanism of the texture in the XY-scan, although similar textures were developed in L-PBF and EB-PBF. In the XY-scan of EB-PBF, because the vertically grown columnar cells can assist the epitaxial growth in the above layers to decrease the nucleation energy, their fraction is further increased after several layer processes, thus forming the same <100> texture in the build direction as that in the X-scan.

However, in the XY-scan of L-PBF, the obliquely grown columnar cells cease to grow in the next layer because their angle with the temperature gradient direction exceeds 45°, which does not favor epitaxial growth. Then, only the vertically and horizontally grown columnar cells remain after several layer processes, forming a <100> texture in the build direction, as explained in previous papers [22,25,52]. The clarified

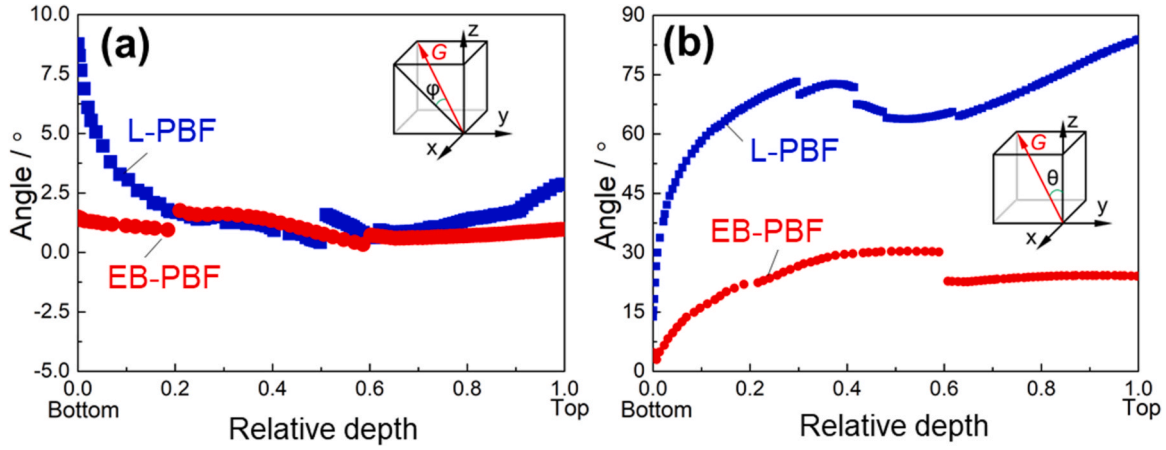

Fig. 14. Angle variation of the temperature gradient direction at the initial solidification position of the melt pool relative to (a) the *yz*-plane, and (b) the build direction in the center of the scan track of EB-PBF and L-PBF.

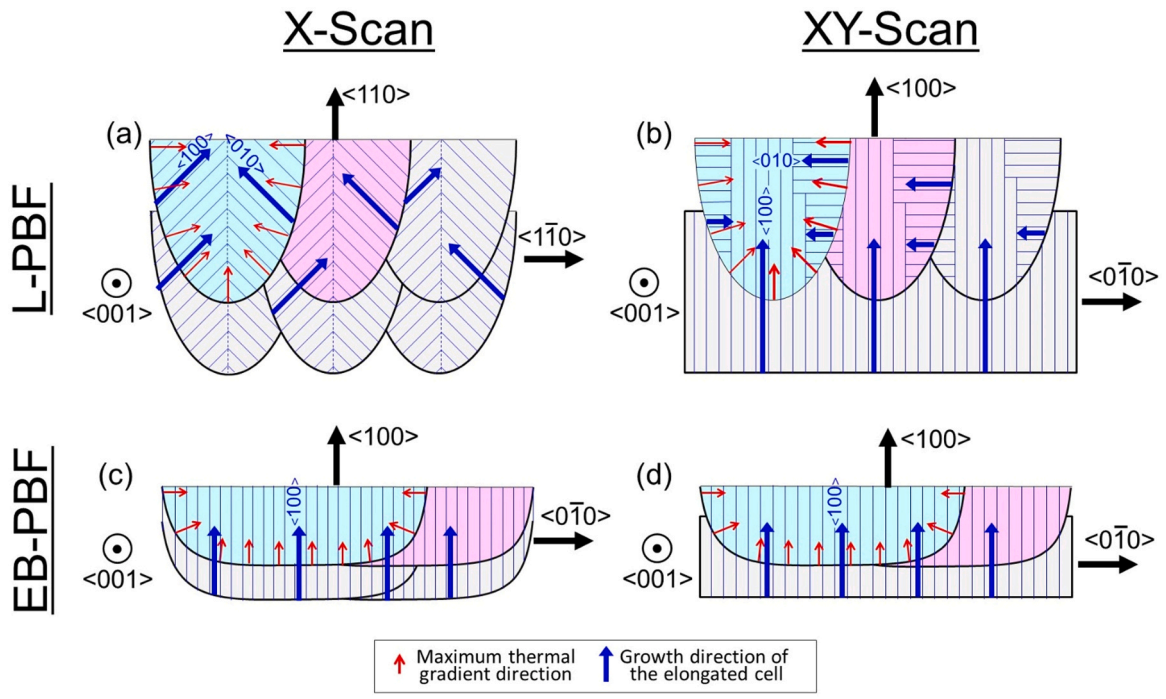

Fig. 15. Schematics showing the differences in the evolution behavior of the crystallographic texture between L-PBF [22] and EB-PBF. (a) X-scan in L-PBF, (b) XY-scan in L-PBF, (c) X-scan in EB-PBF, and (d) XY-scan in EB-PBF.

differences in the evolution behavior of the texture between L-PBF [22] and EB-PBF are schematically shown in Fig. 15.

Based on the discussion, it was clarified that the melt-pool shape plays an important role in texture development, which causes the formation of different textures in L-PBF and EB-PBF in X-scan. The narrow and deep melt pools in L-PBF enable the variation in the crystallographic orientation in the build direction by changing the scanning strategy. This implies that L-PBF is more flexible than EB-PBF for controlling the mechanical properties of the fabricated alloys via crystallographic texture control.

4.2. *Effect of thermal history on the secondary phase formation*

To improve the conductivity of the powders to avoid the smoking phenomenon caused by charge accumulation, an additional preheating process is required in every layer of EB-PBF, wherein the powders are slightly sintered via a scan of the defocused beam at a high speed. Thus, the additional preheating process in EB-PBF significantly affects the thermal history of EB-PBF and L-PBF. The cooling rate in EB-PBF was considered slower than that in L-PBF because of its higher ambient temperature because of preheating. Also, the preheating process can maintain the early built part in EB-PBF at high temperatures until the completion of fabrication. This is similar to the aging process, which changes the microstructure. Microstructure variations caused by the preheating process have been found in several alloys with multiple phases, such as TiAl alloy [13], Ti–6Al–4V alloy [53], Co–Cr–Mo alloy [54], and Inconel 718 [21]. A previous study that used single crystals reported that the β-phase in the Ti–15Mo–5Zr–3Al alloy is stable after short-term aging at 300 and 400 °C for 1.2 ks. The ω-phase and α-phase precipitations require long-term aging at 300 °C for 300 ks and 400 °C for 300 ks, respectively [29]. However, because the preheating temperature during the EB-PBF was as high as 520 °C, metastably forming

an α-phase and a small amount of isothermal ω-phase in the EB-PBF samples is plausible, even after short-term aging by preheating.

The α-phase exists on the columnar cell boundaries and in the vicinity of some melt-pool boundaries, as shown in Fig. 8(a), which may be related to the segregation of Al at these locations during the solidification of the melt pools. The segregation coefficient—the ratio between the Al in the liquid and solid—of Al in the Ti–10V–2Fe–3Al alloy is 1.13 [55], enabling segregation. Al as the formation element of the α-phase is well known, and the high Al content in the local region promotes the formation of the α-phase during the aging process.

Based on these results with respect to precipitate behavior, it is proposed that EB-PBF may be more suitable for fabricating precipitate-strengthened materials, such as Inconel 718. The strengthening phase in Inconel 718 can precipitate directly during the fabrication process [21]. In contrast, L-PBF may be more suitable for producing materials with metastable phases, such as the present Ti–15Mo–5Zr–3Al alloy, in which the material is quickly cooled to restrain the undesired phase transformation, because the precipitation of the α-phase largely degrades the ductility, as shown in Fig. 11. Rapid cooling of L-PBF is also beneficial for achieving super-solid solutions by suppressing elemental segregation, resulting in solid solution strengthening in a high-entropy alloy [56]. In the actual application of a product, the influence of geometry and build layout also affects the microstructure, as it affects the heat accumulation behavior during the fabrication process. Hence, this must be considered.

This study clarifies that, in addition to the effect on precipitate behavior, the texture formation behavior also varies between EB-PBF and L-PBF, as described earlier in Section 4.1. These features must be extensively considered when selecting an appropriate AM method for metallic materials.

5. Conclusions

We compared the microstructure, texture, and mechanical properties of the β-type Ti–15Mo–5Zr–3Al alloy fabricated by using EB-PBF and L-PBF. Our major findings are summarized as follows:

1) The fabrication of the specimens with flat surfaces in EB-PBF required a higher scanning speed and lower volume energy density in comparison with those in L-PBF because of the higher energy absorptivity of the electron beam and the additional preheating process in EB-PBF.
2) Despite that the relative density increased with an increase in energy density in the EB-PBF-built specimens, the relative density of the L-PBF-built specimens decreased at higher energy densities because the melting mode transformed from the conduction mode to the keyhole mode at higher energy densities in L-PBF, entrapping the gas during the collapse of the keyhole-type melt pools.
3) The crystallographic texture formation region was considerably wider in EB-PBF than in L-PBF.
4) Both EB-PBF and L-PBF obtained a cubic crystallographic texture via bidirectional scanning, with a 90° rotation in each layer. However, their texture formation mechanisms varied. The <001> texture in the build direction was derived mainly from the vertically grown columnar cells in the EB-PBF-built specimens, whereas it was derived from both the vertically and horizontally grown columnar cells in the L-PBF-built specimens. This is because wide and shallow melt pools were formed in the EB-PBF, and narrow and deep melt pools were formed in L-PBF.
5) Because of the difference in the melt pools described in 4), the crystallographic texture developed in the X-scan samples varied for the EB-PBF- and L-PBF-built specimens. The <110> and <100> aligned textures along the build direction were developed in L-PBF and EB-PBF, respectively.
6) Stacking fault-like α″-phases existed in both the EB-PBF- and L-PBF-built specimens. However, the α-phase existed only in the EB-PBF-built specimens because of the in-situ aging effects in the EB-PBF. It was mainly located on the columnar cell boundaries and in the vicinity of some melt-pool boundaries.
7) The L-PBF-built specimen exhibited significantly better ductility, but a slightly lower strength than that of the EB-PBF-built specimen under the conditions of stronger crystallographic texture and higher relative density.
8) Under the appropriate fabrication conditions, L-PBF is more suitable for producing materials that may form metastable phases, such as the present Ti–15Mo–5Zr–3Al alloy, in which the material is cooled quickly to restrain the undesired phase transformation. Meanwhile, EB-PBF is more suitable for fabricating precipitate-strengthened materials, such as Inconel 718. However, the texture variation must also be considered when selecting an appropriate AM method, depending on the application.

CRediT authorship contribution statement

Shi-Hai Sun: Investigation, Data curation, Validation, Visualization, Writing – original draft, Writing – review & editing. **Koji Hagihara**: Investigation, Methodology, Writing – review & editing. **Takuya Ishimoto**: Investigation, Methodology, Writing – review & editing. **Ryoya Suganuma**: Investigation. **Yun-Fei Xue**: Supervision, Writing – review & editing. **Takayoshi Nakano**: Conceptualization, Writing – review & editing, Supervision, Project administration, Funding acquisition.

Declaration of Competing Interest

The authors declare that they have no known competing financial interests or personal relationships that could have appeared to influence the work reported in this paper.

Acknowledgments

This work was supported by a Grant-in-Aid for Scientific Research (JP18H05254) from the Japan Society for the Promotion of Science (JSPS). This work was also partially supported by the Cross-Ministerial Strategic Innovation Promotion Program (SIP), Materials Integration for Revolutionary Design System of Structural Materials, Domain C1: “Development of Additive Manufacturing Process for Ni-based Alloy” from the Japan Science and Technology Agency (JST).

Appendix A. Supplementary material

Supplementary data associated with this article can be found in the online version at doi:10.1016/j.addma.2021.102329.

References

[1] D. Herzog, V. Seyda, E. Wycisk, C. Emmelmann, Additive manufacturing of metals, Acta Mater. 117 (2016) 371–392.
[2] T. DebRoy, H.L. Wei, J.S. Zuback, T. Mukherjee, J.W. Elmer, J.O. Milewski, A. M. Beese, A. Wilson-Heid, A. De, W. Zhang, Additive manufacturing of metallic components – process, structure and property, Prog. Mater. Sci. 92 (2018) 112–224.
[3] L.E. Murr, E. Martinez, K.N. Amato, S.M. Gaytan, J. Hernandez, D.A. Ramirez, P. W. Shindo, F. Medina, R.B. Wicker, Fabrication of metal and alloy components by additive manufacturing: examples of 3D materials science, J. Mater. Res. Technol. 1 (2012) 42–54.
[4] V. Bhavar, P. Kattire, V. Patil, S. Khot, K. Gujar, R. Singh, A review on powder bed fusion technology of metal additive manufacturing. Additive Manufacturing Handbook, CRC Press, 2017, pp. 251–253.
[5] C. Köroner, Additive manufacturing of metallic components by selective electron beam melting – a review, Int. Mater. Rev. 61 (2016) 361–377.
[6] F. Dausinger, J. Shen, Energy coupling efficiency in laser surface treatment, ISIJ Int. 33 (1993) 925–933.
[7] E. Beyer, K. Wissenbach, Oberflächenbehandlung mit Laserstrahlung, Springer-Verlag, 2013.
[8] M.A. Lodes, R. Guschlbauer, C. Körner, Process development for the manufacturing of 99.94% pure copper via selective laser melting, Mater. Lett. 143 (2015) 298–301.

[9] T. Kolb, F. Huber, B. Akbulut, C. Donocik, N. Urban, D. Maurer, J. Franke, Laser beam melting of NdFeB for the production of rare-earth magnets, in: Proceedings of the Electric Drives Production Conference (EDPC), IEEE, 2016, pp. 34–40.

[10] H.J. Gong, K. Rafi, H.F. Gu, T. Starr, B. Stucker, Analysis of defect generation in Ti–6Al–4V parts made using powder bed fusion additive manufacturing processes, Addit. Manuf. 1–4 (2014) 87–98.

[11] A. Townsend, N. Senin, L. Blunt, R.K. Leach, J.S. Taylor, Surface texture metrology for metal additive manufacturing: a review, Precis. Eng. 46 (2016) 34–47.

[12] J. Beuth, J. Fox, J. Gockel, C. Montgomery, R. Yang, H.P. Qiao, E. Soylemez, P. Reeseewatt, A. Anvari, S. Narra, N. Klingbeil, Process mapping for qualification across multiple direct metal additive manufacturing processes, in: Proceedings of the Solid Freeform Fabrication Symposium, University of Texas, Austin, 2013, pp. 655–665.

[13] M. Todai, T. Nakano, T. Liu, H.Y. Yasuda, K. Hagihara, K. Cho, M. Ueda, M. Takeyama, Effect of building direction on the microstructure and tensile properties of Ti-48Al-2Cr-2Nb alloy additively manufactured by electron beam melting, Addit. Manuf. 13 (2017) 61–70.

[14] L. Loeber, S. Biamino, U. Ackelid, S. Sabbadini, P. Epicoco, P. Fino, J. Eckert, Comparison of selective laser and electron beam melted titanium aluminides, in: Proceedings of the Solid Freeform Fabrication Symposium, Austin, TX, USA, 2011, pp. 547–556.

[15] A.S. Wu, D.W. Brown, M. Kumar, G. Gallegos, W.E. King, An experimental investigation into additive manufacturing induced residual stresses in 316L stainless steel, Metall. Mater. Trans. A 45 (2014) 6260–6270.

[16] Y.J. Liu, S.J. Li, H.L. Wang, W.T. Hou, Y.L. Hao, R. Yang, T.B. Sercombe, L. C. Zhang, Microstructure, defects and mechanical behavior of beta-type titanium porous structures manufactured by electron beam melting and selective laser melting, Acta Mater. 113 (2016) 56–67.

[17] X.L. Zhao, S.J. Li, M. Zhang, Y.D. Liu, T.B. Sercombe, S.G. Wang, Y.L. Hao, R. Yang, L.E. Murr, Comparison of the microstructures and mechanical properties of Ti–6Al–4V fabricated by selective laser melting and electron beam melting, Mater. Des. 95 (2016) 21–31.

[18] Y. Zhong, L.E. Rännar, S. Wikman, A. Koptyug, L.F. Liu, Daqing Cuia, Z.J. Shen, Additive manufacturing of ITER first wall panel parts by two approaches: selective laser melting and electron beam melting, Fusion Eng. Des. 116 (2017) 24–33.

[19] K.N. Amato, J. Hernandez, L.E. Murr, E. Martinez, S.M. Gaytan, P.W. Shindo, S. Collins, Comparison of microstructures and properties for a Ni-base superalloy (alloy 625) fabricated by electron and laser beam melting, J. Mater. Sci. Res. 1 (2012) 3–41.

[20] S.H. Sun, Y. Koizumi, S. Kurosu, Y.P. Li, H. Matsumoto, A. Chiba, Build direction dependence of microstructure and high-temperature tensile property of Co–Cr–Mo alloy fabricated by electron beam melting, Acta Mater. 64 (2014) 154–168.

[21] S.H. Sun, Y. Koizumi, T. Saito, K. Yamanaka, Y.P. Li, Y.J. Cui, A. Chiba, Electron beam additive manufacturing of Inconel 718 alloy rods: impact of build direction on microstructure and high-temperature tensile properties, Addit. Manuf. 23 (2018) 457–470.

[22] T. Ishimoto, K. Hagihara, K. Hisamoto, S.H. Sun, T. Nakano, Crystallographic texture control of beta-type Ti–15Mo–5Zr–3Al alloy by selective laser melting for the development of novel implants with a biocompatible low Young's modulus, Scr. Mater. 132 (2017) 34–38.

[23] S.H. Sun, T. Ishimoto, K. Hagihara, Y. Tsutsumi, T. Hanawa, T. Nakano, Excellent mechanical and corrosion properties of austenitic stainless steel with a unique crystallographic lamellar microstructure via selective laser melting, Scr. Mater. 159 (2019) 89–93.

[24] P. Wang, P. Huang, F.L. Ng, W.J. Sin, S. Lu, M.L.S. Nai, Z. Dong, J. Wei, Additively manufactured CoCrFeNiMn high-entropy alloy via pre-alloyed powder, Mater. Des. 168 (2019), 107576.

[25] S.H. Sun, K. Hagihara, T. Nakano, Effect of scanning strategy on texture formation in Ni-25 at% Mo alloys fabricated by selective laser melting, Mater. Des. 140 (2018) 307–316.

[26] H.L. Wei, J. Mazumder, T. DebRoy, Evolution of solidification texture during additive manufacturing, Sci. Rep. 5 (2015) 16446.

[27] A. Takase, T. Ishimoto, R. Suganuma, T. Nakano, Surface residual stress and phase stability in unstable β-type Ti-15Mo-5Zr-3Al alloy manufactured by laser and electron beam powder bed fusion technologies, Addit. Manuf. 47 (2021), 102257.

[28] P.R. Boyer, G. Welsh, E.W. Collings, Materials Properties Handbook: Titanium Alloys, ASM International, Materials Park, OH, 1994.

[29] S.H. Lee, K. Hagihara, T. Nakano, Microstructural and orientation dependence of the plastic deformation behavior in β-type Ti–15Mo–5Zr–3Al alloy single crystals, Metall. Mater. Trans. A 43A (2012) 1588–1597.

[30] R. Huiskes, H. Weinans, B. Van Rietbergen, The relationship between stress shielding and bone resorption around total hip stems and the effects of flexible materials, Clin. Orthop. Relat. Res. 274 (1992) 124–134.

[31] M. Tane, K. Hagihara, M. Ueda, T. Nakano, Y. Okuda, Elastic-modulus enhancement during room-temperature aging and its suppression in metastable Ti-Nb-based alloys with low body-centered cubic phase stability, Acta Mater. 102 (2016) 373–384.

[32] S.H. Lee, M. Todai, M. Tane, K. Hagihara, H. Nakajima, T. Nakano, Biocompatible low Young's modulus achieved by strong crystallographic elastic anisotropy in Ti–15Mo–5Zr–3Al alloy single crystal, J. Mech. Behav. Biomed. Mater. 14 (2012) 48–54.

[33] J.Y. Rho, T.Y. Tsui, G.M. Pharr, Elastic properties of human cortical and trabecular lamellar bone measured by nanoindentation, Biomaterials 18 (1997) 1325–1330.

[34] M. Tane, Y. Okuda, Y. Todaka, H. Ogi, A. Nagakubo, Elastic properties of single-crystalline ω phase in titanium, Acta Mater. 61 (2013) 7543–7554.

[35] J.C. Williams, B.S. Hickman, D.H. Leslie, The effect of ternary additions on the decomposition of metastable beta-phase titanium alloys, Metall. Trans. 2 (1971) 477–484.

[36] S. Ohtani, M. Nishigaki, Effect of Zr on the stability of a Ti-15 Mo base beta alloy, J. Jpn. Inst. Met. 35 (1971) 97–102.

[37] F.F. Cardoso, P.L. Ferrandini, E.S.N. Lopes, A. Cremasco, R. Caram, Ti–Mo alloys employed as biomaterials: effects of composition and aging heat treatment on microstructure and mechanical behavior, J. Mech. Behav. Biomed. Mater. 32 (2014) 31–38.

[38] H.S. Carslaw, J.C. Jaeger. Conduction of Heat in Solids, second ed., Oxford University Press, Oxford, 1986.

[39] K. Dai, L. Shaw, Finite element analysis of the effect of volume shrinkage during laser densification, Acta Mater. 53 (2005) 4743–4754.

[40] A. Takase, T. Ishimoto, R. Suganuma, T. Nakano, Lattice distortion in selective laser melting (SLM)-manufactured unstable β-type Ti-15Mo-5Zr-3Al alloy analyzed by high-precision X-ray diffractometry, Scr. Mater. 201 (2021), 113953.

[41] N.G. Shen, K. Chou, Thermal modeling of electron beam additive manufacturing process: powder sintering effects, in: Proceedings of ASME 2012 International Manufacturing Science and Engineering Conference, ASME MSEC2012-7253, 2012, pp.287-295.

[42] D.Y. Zhang, W.D. Wang, Y.W. Guo, S.T. Hu, D.D. Dong, R. Poprawe, J. H. Schleifenbaum, S. Ziegler, Numerical simulation in the absorption behavior of Ti6Al4V powder materials to laser energy during SLM, J. Mater. Process. Technol. 268 (2019) 25–36.

[43] S.A. Khairallah, A.T. Anderson, A. Rubenchik, W.E. King, Laser powder-bed fusion additive manufacturing: physics of complex melt flow and formation mechanisms of pores, spatter, and denudation zones, Acta Mater. 108 (2016) 36–45.

[44] M. Rombouts, J.P. Kruth, L. Froyen, P. Mercelis, Fundamentals of selective laser melting of alloyed steel powders, CIRP Ann. 55 (2006) 187–192.

[45] K. Hagihara, T. Nakano, H. Maki, Y. Umakoshi, M. Ninomi, Isotropic plasticity of β-type Ti-29Nb-13Ta-4.6Zr alloy single crystals for the development of single crystalline β-Ti implants, Sci. Rep. 6 (2016) 29779.

[46] Y.W. Chai, H.Y. Kim, H. Hosoda, S. Miyazaki, Interfacial defects in Ti-Nb shape memory alloys, Acta Mater. 56 (2008) 3088–3097.

[47] J. Hernandez, S.J. Li, E. Martinez, L.E. Murr, X.M. Pan, K.N. Amato, X.Y. Cheng, F. Yang, C.A. Terrazas, S.M. Gaytan, Y.L. Hao, R. Yang, F. Medina, R.B. Wicker, Microstructures and hardness properties for β-phase Ti-24Nb-4Zr-7.9Sn alloy fabricated by electron beam melting, J. Mater. Sci. Technol. 29 (2013) 1011–1017.

[48] W. Chen, C. Chen, X.H. Zi, X.F. Cheng, X.Y. Zhang, Y.C. Lin, K.C. Zhou, Controlling the microstructure and mechanical properties of a metastable β titanium ally by selective laser melting, Mater. Sci. Eng. A 726 (2018) 240–250.

[49] D.D. Gu, B.B. He, Finite element simulation and experimental investigation of residual stresses in selective laser melted Ti-Ni shape memory alloy, Comput. Mater. Sci. 117 (2016) 221–232.

[50] M.J. Lai, C.C. Tasan, D. Raabe, On the mechanism of {332} twinning in metastable β titanium alloys, Acta Mater. 111 (2016) 173–186.

[51] S. Ehtemam Haghighi, H.B. Lu, G.Y. Jian, G.H. Cao, D. Habibi, L.C. Zhang, Effect of α″ martensite on the microstructure and mechanical properties of beta-type Ti-Fe-Ta alloys, Mater. Des. 76 (2015) 47–54.

[52] T. Ishimoto, K. Hagihara, K. Hisamoto, T. Nakano, Stability of crystallographic texture in laser powder bed fusion: understanding the competition of crystal growth using a single crystalline seed, Addit. Manuf. 43 (2021), 102004.

[53] X.P. Tan, Y. Kok, Y.J. Tan, M. Descoins, D. Mangelinck, S.B. Tor, K.F. Leong, C. K. Chua, Graded microstructure and mechanical properties of additive manufactured Ti–6Al–4V via electron beam melting, Acta Mater. 97 (2015) 1–16.

[54] S.H. Sun, Y. Koizumi, S. Kurosu, Y.P. Li, A. Chiba, Phase and grain size inhomogeneity and their influences on creep behavior of Co–Cr–Mo alloy additive manufactured by electron beam melting, Acta Mater. 86 (2015) 305–318.

[55] A. Mitchell, A. Kawakami, Segregation and solidification in titanium alloys, in: Proceedings of the Ti-2007 Science and Technology, The Japan Institute of Metals, 2007, pp. 173–176.

[56] T. Ishimoto, R. Ozasa, K. Nakano, M. Weinmann, C. Schnitter, M. Stenzel, A. Matsugaki, T. Nagase, T. Matsuzaka, M. Todai, H.S. Kim, T. Nakano, Development of TiNbTaZrMo bio-high entropy alloy (BioHEA) super-solid solution by selective laser melting, and its improved mechanical property and biocompatibility, Scr. Mater. 194 (2021), 113658.